Chemically-oscillating reactions during the diagenetic oxidation of organic matter and in the formation of granules in late Paleoproterozoic chert from Lake Superior

DOMINIC PAPINEAU[1,2,3], ZHENBING SHE[4], MATTHEW S. DODD[1,2,3]

1 London Centre for Nanotechnology, 17-19 Gordon Street, University College London, London, UK.

2 Department of Earth Sciences, University College London, London, UK.

3 Centre for Planetary Sciences, University College London, London, UK.

4 School of Earth Sciences, China University of Geosciences, Wuhan, China.

Revised manuscript submitted for publication in *Chemical Geology*

Abstract (380 words)

Filamentous and coccoidal microfossils have been reported since the 1950's from a range of granular cherts from the Late Paleoproterozoic southwestern Superior Craton, Canada-United States. However, the chemical and mineral compositions of granules, the presence of microfossils in granules, and the common presence of granules in intercolumnar space of stromatolitic chert are poorly documented and explained. Furthermore, the depositional model for the origin of granules in wave-agitated waters does not entirely explain their mineral diversity nor their characteristic morphologies and patterns. We report on the crystallinity of organic matter, mineral diversity, and compositions of microfossils in granules from three different kinds of late Paleoproterozoic cherts, namely phosphatic, organic, and haematitic. Stromatolitic organic-rich chert from the Gunflint Fm contains granules with euhedral carbonate and equidistant concentric laminations of organic matter, akin to fractal patterns from the Belouzov-Zhabotinsky (B-Z) chemically-oscillating reaction. These granules also contain authigenic anatase, ferric-ferrous silicates, and Fe-oxides. Filamentous and coccoidal microfossils similar to those of the Gunflint occur in chert from the Biwabik Formation and share morphology, and co-occur with Mn-siderite and apatite. Granules in phosphatic chert in the Michigamme Formation often contain filamentous and coccoidal microfossils composed of organic matter, sericite, and apatite. Bulk carbonate associated with these Michigamme granular phosphatic chert beds has systematically negative $\delta^{13}C_{carb}$ values around -3.1 ± 0.9 ‰ (1σ) and $\delta^{18}O_{carb\text{-}SMOW}$ between +20.8 and +30.7‰, which suggest some contribution from the diagenetic oxidation of organic matter. Notably, residual carboxylic acid is detectable in C-XANES spectra of organic matter from granular phosphatic chert, which is a residual reactant of B-Z type reactions. Along with previously reported observations of pyritised microfossils from the Gunflint Formation, these distinct mineralogies indicate variable

modes of preservation for the products of chemically-oscillating reactions that likely relate to the availability of different oxidants in the diagenetic environment. We conclude that the Late Paleoproterozoic shallow-marine environments of the Lake Superior area were populated by morphologically similar micro-organisms, and that the diagenetic oxidation of organic matter through chemically-oscillating reactions contributed to the formation of spheroidal rosettes, granules, and concretions during a late Paleoproterozoic Great Putrefaction Event. Diagenetic spheroids in chert that contain organic matter or microfossils thus provide a reliable petrographic context to search for a record of putrefaction of microbial life on the early Earth and on other ancient planetary surfaces.

Keywords: phosphorite, jasper, apatite, Proterozoic, organic matter, carbon isotopes, concretion, granule, Raman, XANES

Highlights: 3-5 bullet point 125 characters each

1- Microfossils are sometimes preserved in granules from Late Paleoproterozoic chert in Lake Superior area.

2- Diagenetic carbonate in Michigamme chert associated with apatite granules has negative $\delta^{13}C$ values.

3- Some minerals in granules form from precursor reaction products.

4- Carboxyl in biomass likely plays a role in chemically-oscillating reactions.

5- Chemically-oscillating reactions need to be considered in future interpretations of diagenetic spheroids.

1. Introduction

After the end of the greatest unprecedented perturbation in the carbon cycle (the Lomagundi-Jatuli Event or LJE) and associated Great Oxidation Event (GOE) about two billion years ago (Karhu and Holland, 1996), a number of biological evolutionary changes took place in Earth's biosphere (Papineau, 2010). This is the time when unusual mineralogies associated with stromatolites, granules, and microfossils first became widespread. These biologically-influenced rock types include organic-rich, haematitised, phosphatised, and pyritised stromatolitic and granular cherts in a range of marine environments, including some in proximity to hydrothermal activity. However, there is still no satisfactory comprehensive model for the formation of granular chert that relates their mineralogy, geochemistry, sedimentology, and micropaleontology. For example, rounded granules present in ferruginous cherts have been interpreted as detrital or re-worked structures formed in high-energy environments, with wave action causing the rounded morphology of granules. Many arguments to support this model have been used over the years and include: 1) the similarity of granules with carbonate oolites, which have internal concentric structures and form in shallow-marine wave-agitated water (Lougheed, 1983; Sommers et al., 2000), although oolites in themselves are increasingly regarded as a product of biological activity (Brehm et al., 2003; Pacton et al., 2012), 2) the narrow size range of observed granules, typically from a few hundred microns to a few millimetres, thought to indicate water-based sorting, 3) the observation of desiccation cracks, fractures or plastic deformation features suggest that granules were fully-formed and either plastic or brittle before final deposition (Lougheed, 1983), 4) the occurrence of haematite granules associated with algal fragments and detrital quartz grains suggest a dynamic shallow water environment (Gruner, 1946; French, 1968), 5) and their common association with siliciclastic sedimentary rocks. However, many of these observations could also be explained by concretionary-type growth of granules, for instance during the diagenetic oxidation of organic matter (OM), such as during putrefaction.

A chemically-oscillating reaction known since the 1950's, the Belousov-Zhabotinsky (B-Z from hereon) reaction, involves the spontaneous out-of-equilibrium oxidation of the carboxylic acid malonate with bromate-bromine and sulphate. Under standard conditions, this reaction is known to produce characteristic, millimetre to decimetre in size, fractal patterns of concentric circles, rounded or curved equidistant laminations, spirals, individual single spots, and cavity-like structures, variably accompanied by CO_2 bubbles (Fig. 1). While some of those patterns are akin to those found in agate geodes, the single-spot patterns in particular (Fig. 1e, 1f) are akin to millimetric to centimetric ooids and peloids. Such spontaneous reactions could occur during sedimentary diagenesis as ferric oxides and other oxidants can contribute to oxidise organic remains. This organic oxidation, or putrefaction, might be facilitated by the presence of extracellular polymeric substances derived from microorganisms. The concentric nature of many granules (e.g. Lougheed et al., 1989; Maliva et al., 2005) combined with common outward-radiating acicular crystal further suggest the possibility of an internal or authigenic process of formation for at least some granules. Chemically-oscillating experiments thus show that fractal patterns occur in millimetre to centimetre sizes and that they share similarities with some features in the rock record.

Wave-action is unlikely to produce delicate curved equidistant laminations often seen in granules. Any formational model for granules should also be compatible with the observed carbonate minerals in these structures from chert and associated Banded Iron Formations (BIF) and Iron Formations (IF) that have systematically negative $\delta^{13}C_{carb}$ values, which is an important clue consistent with the oxidation of OM during diagenesis (e.g. Heimann et al., 2010). During the degradation of biomass, chemicals such as HCO_3^-, HS^-, NH_4^+, and PO_4^{3+} are released and hence could become mineralised in carbonates, sulphides, phyllosilicates, and phosphates as concentrically-layered diagenetic spheroids. We thus aim to test a new model for granule formation, which recognises the facts that biomass is rich in carboxylic acids (as they are found in phospholipids, amino acids, and intermediary metabolites) and that various oxidants can occur in different oxidation states in the environment, thereby setting the stage for out-of-equilibrium conditions such as those illustrated in Fig. 1.

In general, granules are taken here to be millimetre-size sub-spheroidal structures with distinct concentric mineral layers in chert, and often between stromatolite columns or in horizons above stromatolite beds. In haematitic chert (i.e. jasper), laminations are dominated by haematite (Lougheed, 1983), whereas in organic-rich chert, laminations in granules are composed of OM (Lanier, 1989). Granule interiors are often coarse-grained and because of their variable concentricity and mineralogy, they have been alternatively referred to as peloids (e.g. Knoll and Simonson, 1981; Lanier, 1989; Hiatt et al., 2015), pisoids (e.g. Simonson, 1985), and ooids (e.g. Hofmann, 1972; Buick, 1992; Sommers et al., 2000). These reports document diverse types of microscopic rounded structures with interiors characterised by various minerals, grain sizes, and textures, which are collectively grouped here and called 'granules'.

The objective of this study is to provide a comprehensive geochemical and sedimentological documentation of mineralogically different granular cherts in order to better understand both the biological and non-biological processes of putrefaction and the possible role of chemically-oscillating reaction in organic-rich siliceous oozes. The focus of this study is on late Paleoproterozoic granular cherts from the southwestern margin of the Superior Craton, namely from the near-synchronous Michigamme, Biwabik, and Gunflint Formations. Granular cherts of nearly the same age from a unique region hold the potential to preserve evidence for how the oxygenation of surface environments resulted in the preservation of diagenetic structures and the preservation of microfossils.

2. Geology and samples

During the accretion of supercontinent Nuna (Laurentia) in the SW Superior Craton, the Penokean Orogeny resulted in the closure of the Baraga Basin in the Marquette range.

These events took place between 1.85 and 1.83 Ga (see Shultz and Cannon (2007) and references therein) and resulted in the closing of many coeval basins with hydrothermal activity that delivered vast quantities of Fe on the seafloor, now preserved as Banded Iron Formations (BIFs) of the Cuyuna, Mesabi, Iron River, Marquette, Gogebic, and Gunflint ranges (Fig. 2a). The Penokean Orogen is thought to have ended by 1.84 Ga (Schneider et al., 2002) and to have resulted in the suture of island arcs and the Wisconsin Magmatic Terrain south of the Superior Craton (Van Wyck and Johnson, 1997). Regional volcanism at 1.88 Ga (Rasmussen et al., 2012) was swiftly followed by widespread hydrothermal activity and the deposition of late Paleoproterozoic BIFs. Notably, if the younger rocks of the 1.15 to 1.10 Ga mid-continental rift (Heaman et al., 2007) are removed from the map in Figure 2a and the Superior BIFs are stitched back together, the time-correlative late Paleoproterozoic BIF-pelite-chert successions of the Cuyuna and Mesabi ranges in Minnesota, the Iron River, Gogebic, and Marquette ranges in Michigan, and the Gunflint range of west Ontario would form a continuous mostly linear belt more than 600 km long (Schulz and Cannon, 2007). The Animikie Group of Ontario and Minnesota thus has an equivalent in the Baraga Group of Michigan such that the Rove Fm is synchronous to the Michigamme Fm (Nelson et al., 2010). The late Paleoproterozoic basins of Michigan's Upper Peninsula have thus been dissected and extended in an aulacogen toward the southeast during the late Mesoproterozoic mid-continental rift leaving the Marquette, Gogebic, and Iron River ranges on the south side of Lake Superior (Ojakangas et al., 2001). Metamorphic grades generally increase towards the southwest such that the Gunflint formation is generally considered to be the least affected by metamorphic recrystallization. Metamorphic grades in the Gunflint Fm are below the lower greenschist facies, whereas the Biwabik and Michigamme formations have been metamorphosed at the sub-greenschist to greenschist facies, respectively. Collectively, the BIFs of the Animikie and Baraga Groups include various types of chert-associated mineralogy and sedimentology, including stromatolitic and granular jasper (Lougheed, 1983; Maliva et al., 2005), cherty stromatolites with grey and red haematite columns (Shapiro and Konhauser, 2015), coarse and fine laminated grey-red Fe-silicate BIFs (i.e. taconite) and grey magnetite cherty BIFs (French, 1968). Age constraints include precise U-Pb ages on zircons, which give an age of 1.878 Ga to 1.836 Ga for tuff beds of the Gunflint Fm and 1.874 Ga for the Hemlock volcanics that intrude the Negaunee Fm below the Michigamme Fm (Fralick et al., 2002; Rasmussen et al., 2012).

Samples in this study come from the Gunflint, Biwabik, and Michigamme formations. Black chert samples from Gunflint Fm (samples *GF-1 and GF-7*) were collected from the type locality at Schreiber Beach (Fig. 2b; Tyler and Barghoorn, 1954). Black cherts from the Gunflint Fm contain unambiguous and exceptionally well-preserved microfossils (Tyler and Barghoorn, 1954; Schopf et al., 1965; Awramik and Barghoorn, 1977; Lanier, 1989; Wacey et al., 2013; 2012; Brasier et al., 2015). In the correlative Biwabik Fm of the Mesabi range in Minnesota (Fig. 2a), there is stromatolitic jasper with columns that vary between about 1 and 3 cm in diameter and intercolumns with haematite-magnetite granules (sample *ME-B1*) (Fig. 2c; Gruner, 1946; Lougheed, 1983; Shapiro and Konhauser, 2015). Samples of concretionary jasper (sample *AG1108*) from Thunderbird mine dumps came from the 'Upper Cherty' member of the Biwabik Fm (Fig. 2d). Lastly, in the Huron River locality at Big Eric's Crossing locality of the Baraga Basin in Michigan's Upper Peninsula, the Michigamme Fm contains silicified argillaceous sedimentary rocks that formed in a shallow-marine environment with decimetre-size stromatolites (Fig. 2e) and centimetre-size apatite concretions (sample *MA0708*) (Fig. 2f). Samples from the *MMTU* drill core (Michigan Technological University) came from the Mulligan Creek locality in the Dead River Basin (Fig. 2a).

3. Analytical methods

3.1. Optical microscopy and μRaman imaging

Optical microscopy was performed with an Olympus BX51 microscope with 4X, 10X, 20X, 50X, and 100X objectives on 30 μm thin sections polished with 0.25 μm Al_2O_3. No oil immersion was used, but Buelher® epoxy was used to make the thin sections. Micro-Raman imaging was performed at the London Centre for Nanotechnology of the University College London with a WITec α300 Confocal Raman Imaging system. A 532 nm laser was used and focused at 200X magnification for large area scans and at up to 1000X for smaller area scans. An optic fiber 50 microns in diameter was used to collect a Raman spectrum at a confocal depth at least 1 micron below the polished surface of the thin section. Each pixel was recorded with a typical dwell time of 0.4 to 0.6 seconds. All Raman spectra were corrected for cosmic rays using the cosmic ray reduction function in the WITec Project Four Plus software. For all presented average Raman spectra, pixels from Raman images were selected on the basis of their nearly identical point spectra and the resulting average spectra were corrected with a background subtraction using polynomial fits typically of order 4, 5 or 6. Raman spectral parameters such as peak positions, Full Width at Half Maximum (FWHM), and areas under the curve were extracted from well-resolved Raman peaks of interest in background-corrected spectra, normalised to the spectral baseline, and then modelled with a Lorenz-fitted equation. To extract crystallisation temperature estimates from Raman spectra (Beyssac et al., 2002) in the Michigamme chert, the following peaks were used: D1 (around 1345 cm^{-1}), G + D2 (around 1605 and 1620 cm^{-1}, respectively). The D3 band at around 1510 cm^{-1} and the D4 band around 1245 cm^{-1} used in the Lahfid et al. (2010) and Kouketsu et al. (2014) geothermometer were expectedly not resolved, but were nevertheless extracted from Lorenz-fitted equations for the Gunflint, Biwabik, and Michigamme formations (Fig. 3; Table 1), where the low crystallization temperatures make this geothermometer more suitable, but still with uncertainties of more than 50^{o}C. Raman hyperspectral images of mineral associations were generated by mapping the main peak intensities (or unique peaks) for specific minerals using the WITec Project Four Plus data processing software; the peaks include those distinct for stilpnomelane (~3620 cm^{-1}), OM (~1600 cm^{-1}), haematite (~1320 cm^{-1}), carbonate (~1090 cm^{-1}), apatite (~965 cm^{-1}), muscovite (~705 cm^{-1}), magnetite (~670 cm^{-1}), rutile (~612 cm^{-1}), quartz (~465 cm^{-1}), and anatase (~138 cm^{-1}). All Raman peak positions were read directly from measured average spectra calculated from representative regions with low signal-to-noise and after background removal.

3.2. Isotope Ratio Mass Spectrometry

Analyses of microdrilled carbonate powders were performed with a Gas Bench heated at 70°C and connected to a ConFlo III system and finally injected into a Delta XL mass spectrometer at the Geophysical Laboratory of the Carnegie Institution for Science. The reproducibility (precision and accuracy) on $\delta^{13}C_{carb}$ and $\delta^{18}O_{carb}$ values[1] was better than ±0.5‰ (1σ) and usually better than ±0.2‰ (1σ) for $\delta^{13}C_{carb}$ values. Accuracy was evaluated on the basis of repeated measurements of internal calcite standard 'Chi' and dolomite 'Tytyri' as well as with a few analyses of NBS 18 and NBS 19. Carbonate carbon isotope data are reported with a 0.1‰ correction and oxygen isotope data were corrected with a 9.7‰ shift, based on the average difference between the measured $\delta^{18}O_{carb}$ of the internal standard standards and their true values, which is due to instrumental/procedural fractionation.

Organic matter was obtained by dissolving about 5 to 10 mg of powder in pre-muffled Ag boats with 10% ultrapure HCl followed by air drying in a laminar air flow hood. The residue was then combusted in a CE2500 Elemental Analyser and injected into a Delta V mass spectrometer through a Conflo III system (Papineau et al., 2013). Reproducibility on $\delta^{13}C_{org}$ values was better than ±0.2‰ (1σ) on standards of Peru mud, acetanilide, and better than ±5% for abundance (1σ) based on the long-term reproducibility of standards.

[1] Carbon and oxygen isotope data are reported in the conventional form $\delta^{13}C_{org}$ or $\delta^{13}C_{carb}$ = $[(^{13}C/^{12}C)_{microdrill}/(^{13}C/^{12}C)_{PDB} - 1] \times 1000$‰ and $\delta^{18}O_{carb} = [(^{18}O/^{16}O)_{microdrill}/(^{18}O/^{16}O)_{SMOW} - 1] \times 1000$‰.

3.3. Scanning Electron Microscopy (SEM) and Energy Dispersive Spectroscopy (EDS)

Analyses by SEM were performed using a JEOL JSM-6480L SEM in the Department of Earth sciences at University College London. Operating conditions for SEM imaging and EDS analysis included a 15kV accelerating voltage for an electron beam current of 1nA, and a working distance of about 10mm. Polished thin sections were cleaned with clean wipes and isopropyl alcohol, dried with dry N_2, before the deposition of a few nanometres of Au (1 or 2 minutes coating under a current of about 1.8 mA in Ar) for analysis in the SEM. Analyses were calculated by the software using ZAF correction and normalized to 100.0 %, which yield an error of about 1%.

3.4. Synchrotron-based Scanning Transmission X-ray microscopy (STXM)

Sample preparation for X-ray absorption near-edge structure (XANES) spectral analysis involved dissolution of whole-rock powder (about 5g) from cherts with a density-calibrated CsF-HF solution (ρ = 1.8 g/cm^3) and dioxane treatment (Alexander et al., 2007). Dioxane was used to generate a separate solution of lower density, which visibly floats on top of the CsF-HF in a clear teflon tube, and thus isolating the acid insoluble OM at the interface between the two solutions. After centrifugation, the acid-insoluble OM was pipetted with sterile disposable plastic pipettes in muffled glass vials, washed twice in 2 M HCl, and rinsed three times in DI water, before drying in a laminar air flow hood. Once dried, small clumps of OM were sampled and mixed with a molten bead of S (~80^{o}C) on a glass slide. Upon cooling, the sulphur crystallized and trapped the acid-insoluble OM. The S bead was subsequently detached from the glass slide and glued onto an epoxy stub and microtomed with a diamond knife into 100 nm slices. Microtome sections of OM were transferred to different 200 mesh Cu TEM grids coated with silicon monoxide. The S was removed by sublimation at ~70^{o}C in air for a few minutes over a hot plate.

Samples were analyzed with the polymer STXM beamline 5.3.2.2. at the Advanced Light Source (ALS), Lawrence Berkeley National Laboratory (Kilcoyne et al., 2003). During analysis, the electron current in the storage ring was held constant in "topoff mode" at 500 mA at energy of 1.9 GeV, providing a nearly constant flux of photons at the STXM end-station. The dispersive and non-dispersive exit slits were set at 25 μm. Focusing of the photon beam is produced by a Fresnel zone plate with a spot size of around 30 nm. STXM data were acquired as spectral image stacks (i.e. a series of X-ray absorption images at sequential energies), from which XANES spectra of regions of interest were extracted. The highest spectral resolution (0.1 eV step between subsequent images) was in the 282-292 eV range, where the near-edge spectral features for electronic transitions from core shell states to anti-bonding σ* and π*-orbitals are located. XANES spectra are presented as the ratio of transmission spectra from the region of interest, I, relative to background transmission spectra, I_0, calculated as $A = -\ln(I/I_o)$.

4. Results

4.1. Crystallinity of organic matter from Gunflint, Biwabik, and Michigamme cherts

Raman spectra for OM in granules from the black chert of the Gunflint Fm show highly disordered OM with a broad D1-band peaking at 1344 cm^{-1} (FWHM between 90 and 130 cm^{-1}) and a sharp and intense G-band between 1603 and 1609 cm^{-1} (FWHM between 45 and 57 cm^{-1}) (Fig. 3a). These features are consistent with the C-XANES spectra for OM in the Gunflint Fm, which include a weak 285 eV absorption for aromatic C=C and resolvable absorptions at 286.8 and 288.6 eV, respectively for aromatic alcohol and carboxyl (De Gregorio et al., 2009). Together with the presence of greenalite and exceptionally-preserved microfossils and granules (Lanier, 1989), these characteristics are consistent with metamorphism at the prehnite-pumpellyite facies and with a complex residual organic structure (Vandenbroucke and Largeau, 2007). This is further supported by the presence of aliphatic functional groups suggested by Raman peaks in the region of 2700-3000 cm^{-1} (Fig. 4j), and consistent with CH_2 and CH_3 bonds detected by FTIR analyses of OM in Gunflint microfossils (Igisu et al., 2009). It is unclear whether the broad fluorescence peak centred near 1400 cm^{-1} represents an analytical artefact, but these have unusually strong Raman scattering in the region expected for OM (Fig. 4m). The metamorphic temperature calculated for OM in the Gunflint Fm is between 200 and 350^{o}C (average of 262 ± 77 ^{o}C) using Lorenz-fitted D- and G-bands and the equations of Lafhid et al. (2010) and Kouketsu et al. (2014) (Fig. 3 and Table 1).

In the Biwabik Fm, OM is frequently associated with haematitic microfossil-like structures, but typically has lower signal-to-noise ratios (Fig. 3c, 3d), which due to the micrometre size of the OM particles. Organic matter from Biwabik has resolvable G-bands between 1569 and 1599 cm^{-1} (with FWHM around 60 cm^{-1}) and D1-bands around 1337-1356 cm^{-1} (with FWHM between 110 and 130 cm^{-1}), which can have interference from the haematite peak around 1320 cm^{-1} (Marshall et al., 2011; 2013). Interference from the haematite peak combined with low signal-to-noise of the spectra prevent reliable determination of crystallization temperatures, here tentatively estimated between 229 and 280^{o}C. These new observations are consistent with the notion that metamorphism from the prehnite-pumpelleyite facies to the greenschist facies shifts the position of the G-band toward lower wavenumbers and the D-band toward higher wavenumbers (Schopf et al., 2006).

Raman spectra of OM associated with apatite coccoids and filaments in the Michigamme cherty phosphorite have intense and narrow D1-bands between 1338 and 1353 cm^{-1} (full width at half maximum (FWHM) between 44 and 65 cm^{-1}) and G-bands between 1567 to 1587 cm^{-1} (FWHM between 41 and 77 cm^{-1}) (Fig. 3e, 3f). These characteristics can be used to estimate the crystallisation temperature using the Beyssac et al. (2002) geothermometer between 352 and 398^{o}C and indicate a 'poorly crystalline graphite' structure for this OM, which is characterized by similarly-shaped narrow and sharp G- and D1-bands (e.g. Papineau et al., 2011). X-ray Absorption Near-Edge Structure (XANES) spectra of OM from this sample revealed significant absorption by the aromatic C=C and C-C bonds, respectively at 285.3 and 291.7 eV (Fig. 4a), consistent with the crystallinity inferred from Raman spectra (Bernard et al., 2009) and with metamorphic grade at the greenschist facies.

4.2. Petrology of stromatolitic and granular organic chert from the Gunflint Formation

The organic-rich stromatolitic and granular chert from the Gunflint Fm in Ontario also contain granules in intercolumnar space and finely disseminated OM preserved in stromatolitic laminae. Stromatolites occur as centimetre-size columns branching in multifurcate and anastomosed columnar morphologies (Fig. 5a-5b), whereas intercolumnar granules are often concentrically-laminated and typically around 500 μm in diameter (Fig. 5c; 5f). Here, the chert is essentially cryptocrystalline throughout and inter-granular outsized carbonate rhombs are up to 400 μm in size. The concentrically-laminated granules contain fine layers of OM about 10 μm in thickness and frequent authigenic-diagenetic euhedral carbonate minerals occur in external layers (Fig. 5g-5j). Some granules contain concentric layers of pyrite (Fig. 5e). Diagenetic euhedral carbonate rhombs also occur in the intergranular spaces between stromatolite columns (Fig. 5k), and these are occasionally replaced by pyrite remobilised from later diagenetic veins (Fig. 5d). Similar euhedral crystals in the Biwabik Fm are composed of gypsum partly replaced by magnetite (Lougheed, 1983). Other large euhedral carbonate crystals several hundred microns in size contain highly fluorescent OM (Fig. 5k-m), analogous to other occurrences from the Gunflint chert where carbonate has been replaced by Fe-oxides (Sommers et al., 2000).

Microscopic filamentous structures and the commonly co-occurring spheroidal structures are relatively common in fine stromatolitic laminations and less common in non-concentrically laminated Gunflint granules (Fig. 6 and 7). Filaments are 2 to 4 μm in diameter with lengths of up to 400 μm and they also occur embedded in the laminae of the stromatolite columns (Fig. 6a-g), all consistent with previous observations (Tyler and Barghoorn, 1954).

They are composed of finely disseminated OM (Fig. 6g) that has the usual spectral characteristic of amorphous OM, but sometimes has highly fluorescent domains (Fig. 6h). Spheroidal organic structures range in size between about 6 and 50 μm and tend to occur in granules where they can be accompanied by filaments (Fig. 7a-d) and more complex reticulated spheroidal structures (Fig. 7e). In one of the studied granules, spheroidal structures between about 10 and 25 μm (Fig. 7f-h) co-occur with diagenetic brown dolomite, which contains OM (Fig. 7i-j).

4.3. Petrology of stromatolitic and granular jasper from the Biwabik Formation

Stromatolitic and granular haematitic chert from the Biwabik Fm is characterized by a similar but chemically distinct diagenetic history to the Gunflint and Michgamme cherts. Jasper from the Mary Ellen mine in the Biwabik Fm contains grey magnetite and red haematite granules (> 200 μm in diameter), which occur between millimetre-size multifurcate and anastomosed stromatolite columns made of finely laminated chert and haematite-rich layers (Fig. 8a-8b). Jasper occurrences in the Thunderbird mine include centimetre-sized concretions that are typically flattened and no greater than about 5 cm in size (Fig. 8c). Granules and concretions are variably composed of finely disseminated, microscopic to nanoscopic red haematite (Fig. 8d-7f). Some granules contain regular patterns of spheroidal haematite structures associated with monazite (Fig. 8e) or central patches of stilpnomelane surrounded by Mn-siderite (Fig. 8f). Fe-oxide minerals that form concentric layers in granules are generally concentrated in layers of similar thickness (Fig. 8g). Some granules are mostly formed of such mixtures of magnetite or haematite with apatite and carbonate both commonly have poikilitic-type textures (Fig. 8h-8k). These authigenic apatite crystals occur as brown subhedral blades more than 100 μm in size and are associated with micron-size particles of OM and carbonate (Fig. 9a-c). Other granules have rims of rounded equidistant laminations of nanoscopic carbonate and interiors of coarse magnetite, fine hematite, and micron-size particles of OM and carbonate (Fig. 9d-9i).

In the chert-hematite matrix of stromatolite columns, there are micron-size apatite grains that occur as isolated euhedral crystals with nanoscopic inclusions of chert and haematite (Fig. 8k). Filamentous and spheroidal microscopic structures occur in some haematite-magnetite granules and concretions (e.g. Fig. 8c) in association with haematite (Fig. 10, 11). Some granules contain patches of filaments with diameters between 0.5 and 4 μm and lengths of hundreds of microns (Fig. 10a-10c). In some other granules, spheroids have sizes typically around 10 μm (Fig. 11a, 11b, 11e), although some spheroids have sizes more than 100 μm (Fig. 11d). Some spheroids also contain microscopic carbonate (Fig. 10d and inset) and/or micron-size particles of OM (Fig. 11i-l). While some peaks of Biwabik OM are mixed with epoxy (Fig. 10f, 11l), as inferred from the presence of peaks at 2854, 2904, and 2952 cm^{-1} –attributable to CH_2 and CH_3 bonds in epoxy, their G-band positions are between 1569 and 1599 cm^{-1}, which indicates an indigenous origin overprinted by sub-greenschist facies metamorphism. Both filamentous and spheroidal structures are composed of finely disseminated red haematite associated with micron-size particles of OM and cross-cutting stilpnomelane (Fig. 11j), which demonstrates their pre-metamorphic origin.

4.4. Petrology of granular phosphatic chert in the Michigamme Formation

Grey chert interlayered with green argillite and carbonate constitutes the main lithologies associated with the Michigamme phosphatic chert at the Mulligan Creek locality. Pyrite and haematite replacing pyrite occur as authigenic disseminations, rosettes, cubes, and occasional massive bands. The dominantly grey chert is banded and often stromatolitic. Chert sometimes occurs as black and white bands and interlayered with argillite rich in OM. Higher in the stratigraphy of the *MMTU* drill core, the chert contains dark grey granules and wrinkly and finely laminated microbial mats of apatite. In the *MMTU* drill core, dolomite occurs as granules, rhombs, cement, matrix micrite, and microcrystalline dolomite beds and veins. Field exposures in Huron River locality reveal the occurrence of coarsely laminated decimetre-scale domal stromatolitic chert (Fig. 2e). Concretions of apatite form pinching and swelling millimetre-long structures and/or centimetre-size sub-ellipsoidal concretionary masses mixed with the matrix of chert (Fig. 2f, 12a-b).

The studied phosphatic chert samples are dominated by microcrystalline quartz (<4μm), carbonate, apatite, disseminations and structures of OM, haematite, and euhedral to anhedral pyrite. Authigenic apatite is systematically associated with OM and appears diffuse with high-relief brown to dark grey patches in transmitted light (e.g. Fig. 12a). Apatite occurs as millimetre- to centimetre-size apatite-sericite concretions (Fig. 12a-12b) and as granules that are typically more than 200 μm in size (Fig. 12d-12i). Granules are usually sub-ellipsoidal and contain disseminated OM that often form a network with a regular pattern (Fig. 12d-12i). There are compartmentalised spheroidal structures around 100 μm in size composed of apatite and OM in the intergranular matrix (Fig. 12j, 12k). Some granules have angular edges that form a sub-hexagonal habit (Fig. 12l-12m) sometimes accompanied by curved equidistant laminations of nanoscopic anatase (Fig. 12n-12o). In some apatite beds (Fig. 12c), there are spheroidal granules of carbonate with fine spheroidally concentric equidistant laminations (Fig. 12p-s) that also contain filaments of OM in their geometric centres (Fig. 12r-s).

Apatite in granules and concretions from these rocks is often associated with OM and muscovite-sericite and often occurs as microscopic filamentous and spheroidal structures (Fig. 13, 14). A millimetre- to centimetre-size concretion of apatite contains distinct filamentous structures more than 200 μm in length and 2 to 6 μm in diameter (Fig. 13a-g). The filaments are composed of OM and apatite and are intermixed with chert, sericite, haematite, and rutile at the micron scale (Fig. 13f, 13g). Micro-Raman imaging shows that OM systematically occurs in the apatite (Fig. 13g-13h), but it also occurs in association with carbonate and chert. Other apatite granules contain a ring of microscopic apatite spheroids each between 10 and 50 μm in size with rims enriched in OM (Fig. 14a-14c). These structures are filled with apatite-sericite, which usually contains OM but sometimes devoid of it, as in the case of euhedral apatite filling some interior (Fig. 14c). A rosette about 60 μm in diameter occurs inside the latter granule and is composed of sub-micron-sized radiating acicular muscovite (sericite). Muscovite was identified from its acicular habit, transparent colour (Fig. 14d), low second order birefringence colours (Fig. 14e), Raman peaks at 198, 266, 705, and at 3629 (for hydroxyl) cm^{-1} (Fig. 14h), and the fact that it contains K, Mg, and Al as detected by EDS. The radiating acicular nature of this rosette, best seen in cross polars (Fig. 14e), and its rim of apatite, best seen in BSE images (Fig. 14f), suggests outward or centrifugal growth. The core of muscovite in this granule is surrounded by an outer layer of quartz (about 80-100 μm thick) with various minerals: spheroidal grains of apatite coated with OM, euhedral anatase crystals 4 to 10 microns in size, and diffuse haematite possibly from weathering (Fig. 14g). The composition of apatite in the Michigamme Fm is fluorapatite with minor levels of rare Earth elements (Table 2). Raman images show the occasional contamination of the thin section by diamonds and epoxy (Fig. 13g-h), but the graphitic OM is indigenous and systematically associated with apatite.

4.5. Isotope and molecular compositions of carbon in the Michigamme Formation

In chert and argillite from the Michigamme Fm at the Mulligan Creek locality (*MMTU* samples), there is typically less than 1.5 wt% of total organic carbon (TOC), and levels average at 0.4 ± 0.4 wt% (1σ) (Fig. 15, Table 3). The $\delta^{13}C_{org}$ values vary between -20.8 and -46.7‰ with an average of -26.2 ± 4.8‰ (1σ). There are only two chert samples that have a $\delta^{13}C_{org}$ value below -35‰ (Fig. 15; Table 3). The pyrite–bearing chert sample at 27.1m has a $\delta^{13}C_{org}$ value of -44.5‰ and occurs just before about 10 metres of stromatolitic chert beds. The chert sample at 3.5m has a $\delta^{13}C_{org}$ value of -46.7‰ and is directly overlain by the first two metres of drill core, which consists of chert-bearing dark grey clumps of apatite seen in all samples above 3.3 m. These observations show that highly ^{13}C-depleted OM can occur before the stratigraphically overlying stromatolites followed by phosphate-rich concretionary-granular chert beds. In comparison, the phosphatic chert from the Huron River locality (*MA0708*) has variable $\delta^{13}C_{org}$ values on millimetre scale between -26.7 and -35.3‰ (Fig. 12b). The carbon isotope composition of carbonate minerals in Michigamme chert is systematically negative and with $\delta^{13}C_{carb}$ values between -1.4 and -5.2‰ with an average of -3.1‰ and 1σ standard deviation of 0.9‰ (Fig. 15; Table 3). These compositions are also characterized by highly ^{18}O-enriched values between +20.7 and +10.8‰, that yield an average $\delta^{18}O_{carb}$ value of +14.8 ± 2.3‰ (1σ).

Acid-insoluble OM from *MA0708* has major C-XANES peaks at 285.3 eV and 291.7 eV (Fig. 4a), typical of OM in Late Paleoproterozoic stromatolitic phosphorites also metamorphosed around the greenschist facies (Papineau et al, 2016). Weak peaks are resolvable at 287.6 and 288.5 eV (Fig. 4a), which independently confirms the presence of residual aliphatic C and carboxyl respectively (Cody et al., 1996; De Gregorio et al., 2011; Bernard et al., 2012). Such pair of peaks has been reported in OM from unmetamorphosed Cretaceous concretionary and organic-rich shales from Germany (Bernard et al., 2012) and from Late Paleoproterozoic stromatolitic phosphorites from the Jhamarkotra Fm (Papineau et al., 2016). The C-XANES spectra for the Michigamme OM are similar to those of OM from the Gunflint Fm (De Gregorio et al., 2009; Alléon et al., 2016) and in fact to OM in general preserved in metamorphosed sedimentary rocks (Bernard et al., 2007; 2009; 2011). The OM analysed also contains N as shown with a peak at 404.0 eV that points to N-bearing functional groups (Cody et al., 2011; Fig. 4b), and O with peaks at 531.7 and 538.9 eV that point to ketone groups (Fig. 4c – Hitchcock and Biron, 1980).

5. Discussion

5.1. Carbon cycling in chert from the Michigamme, Gunflint, and Biwabik formations

Evidence for the diagenetic oxidation of OM in the Michigamme Fm is seen in the systematically negative $\delta^{13}C_{carb}$ values down to -5.2‰, hence a ^{13}C-depleted oxidised source of OM was assimilated by Michigamme carbonate. Most $\delta^{13}C_{org}$ values measured for sedimentary rocks from the Michigamme Fm are within the average composition in the late Paleoproterozoic and, considering the near-zero $\delta^{13}C$ of seawater at that time, these values are therefore consistent with fractionation by the pentose phosphate pathway for CO_2-fixation (Desmarais, 2001; Schidlowski, 2001). For comparison, the Gunflint Fm has similar average $\delta^{13}C_{org}$ value around -27 ‰ and down to -34‰ (Strauss and Moore, 1992). Two samples of chert from the Michigamme Fm have $\delta^{13}C_{org}$ values of -44.5 and -46.7‰ (Fig. 15), which is similar to a small number of analyses from the Gunflint Fm with $\delta^{13}C_{org}$ values down to -45.8‰ that characterise some *Huroniospora*-like microfossils (House et al., 2000). Such highly ^{13}C-depleted values are generally attributed to methane cycling (e.g. Hayes, 1994), and thus observations for the Michigamme Fm possibly point to methanotrophy before a transient episode of stromatolite formation followed by phosphatisation. Similar large ranges of $\delta^{13}C_{org}$ values have been reported from sedimentary rocks from the early Paleoproterozoic Hamersley Group in Western Australia and indicate the co-existence of aerobic shallow waters and anaerobic deep waters (Eigenbrode and Freeman, 2006). Michigamme cherts are thus interpreted to have originated in aerobic shallow-marine sedimentary environments where diagenetic processes associated with OM oxidation included a combination of aerobic heterotrophy, methanotrophy, and possibly other metabolic pathways.

In the black chert from the Gunflint Fm, late diagenetic dolomite rhombs occur as outsized crystals between granules (Fig. 5d) as well as smaller crystals within concentric equidistant laminations of OM (Fig. 5i). Systematically negative bulk $\delta^{13}C_{carb}$ compositions in the Michigamme Fm are similar to siderite-bearing rocks from the Gunflint Fm, down to -5.5‰ (Winter and Knauth, 1992), and to the Biwabik iron formation between -3.7 and -

18.6‰ (Perry et al., 1973) (Table 4). These compositions point to carbonate formation from the product of diagenetically-oxidised OM. The $\delta^{18}O_{SMOW}$ values from the carbonate in Michigamme Fm average at +14.8‰, which is similarly affected by diagenesis as carbonate in the Biwabik Fm with $\delta^{18}O_{SMOW}$ values between +10 and +18‰ (Perry et al., 1973) and the Gunflint Fm with $\delta^{18}O_{SMOW}$ values between +14 and +23‰ (Winter and Knauth, 1992) (Table 4). Euhedral pyrite can replace dolomite during later diagenesis (Fig. 5d) and in concentrically-layered granules of haematite in the Gunflint chert, pyrite has $\delta^{34}S$ value of -1‰ (Fig. 13a in Papineau et al., 2005), which does not unambiguously suggest fractionation by microbial sulphate reduction because mantle sulphur also has this isotopic signature. In brief, diagenetic carbonate produced from the oxidation of biomass is interpreted here to be indicated by the presence of 1) direct association with microfossils (Fig. 7b, 7i, 11d), 2) disseminations inside granules (Fig. 5i, 8f, 8i, 8j, 9b, 9g), 3) rounded equidistant laminations in rims of nanoscopic crystals (Fig. 9g, 10d), 4) spheroidal carbonate granules with rounded equidistant laminations (Fig. 12p-12s), and 5) outsized and zoned intergranular rhombohedral crystals (Fig. 5d, 5k).

The graphitization of OM into graphite is a unidirectional process, and as such the crystallinity of graphitic carbon can be used to estimate crystallization temperatures from Raman D- and G-bands (Beyssac et al., 2002; Lafhid et al., 2010). Metamorphic temperatures derived from Raman spectra of OM in Michigamme cherty phosphorite are between 352 and 398°C, which are consistent with metamorphism at the greenschist facies. The diffuse apatite and OM segregated from chert in filamentous microfossils and spheroids probably acquired this glassy high-relief texture (e.g. Fig. 13d) during such thermal metamorphism. Lower metamorphic temperatures between 209 and 333°C were calculated for the OM in the Gunflint Fm, consistent with other estimates (Alléon et al., 2016) and with prehnite-pumpellyite facies metamorphism. The OM in the Gunflint Fm has three broad peaks at 2649

cm^{-1}, 2934 cm^{-1}, and 3196 cm^{-1} that indicate a better degree of preservation than in the Biwabik and Michigamme formations.

5.2. The variable preservation of spheroidal and filamentous microfossils

The petrography of microfossils in granules and stromatolite laminae from the Gunflint black chert was first described in detail by Tyler and Barghoorn (1954) whose later systematic description became the taxonomic foundation of Precambrian micropaleontology (Barghoorn and Tyler, 1965). It was then recognized that these microfossils could be preserved as primary OM, or be replaced by pyrite, carbonate, or haematite. Both the Biwabik and Michigamme formations contain spheres and filaments that have identical sizes and morphologies to the well-described microfossils from the Gunflint Fm (Awramik and Barghoorn, 1977; Barghoorn and Tyler, 1965; Cloud and Licari, 1968; Knoll and Barghoorn, 1975; Lanier, 1989; Shapiro and Konhauser, 2015; Wacey et al., 2013). The filaments and spheroidal microscopic structures we report from our samples are morphologically similar to the above as well as to haematitic microfossils from late Paleoproterozoic phosphorite (Crosby et al., 2014) and BIF (Karkhanis, 1976; Shapiro and Konhauser, 2015). They are also compositionally distinct from biomimicking structures grown in so-called 'chemical gardens' (Garcia-Ruiz et al., 2017; Barge et al., 2016). The mineralogical preservation of microfossils in chert is thus likely dependent on the abundance of oxidants such as sulphate, oxygen, and/or haematite during diagenesis.

In granules and intergranular matrix of our samples of the Gunflint black chert, typical *Gunflintia minuta* comprises straight to slightly sinuous organic filaments, between 1 and 3 μm in diameter, and up to several hundred microns in length (Fig. 6). Spheroidal microfossils composed of OM range from 3 to 25 μm in diameter (Fig. 7) and they have the typical morphology of *Huroniospora*. Other well-preserved specimens of *Gunflintia* and *Huroniospora* have been analysed *in situ* by SIMS, which reveals similar ranges of $\delta^{13}C$ values between -30 and -38‰ for *Gunflintia* and *Huroniospora* (House et al., 2000; Williford et al., 2013). Such compositions are consistent with the pentose phosphate or acetyl CoA metabolic pathways of CO_2-fixation (House et al., 2003). Morphologically similar microfossils are found in the Michigamme and Biwabik formations, although they have been preserved in different minerals.

In the Michigamme phosphatic chert, spheroidal microfossils composed of OM with apatite occur within granules composed of apatite, chert, muscovite, haematite, and anatase. They occur as spheroidal apatite grains with rims composed of OM and they have diameters between 10 and 50 μm, similar to the multicellular modern cyanobacteria *Chroococcidiopsis sp.* (e.g. Knoll and Barghoorn, 1975). These spheroidal microfossils are generally larger than typical *Huroniospora* or *Myxococcoides*, but they are also similar to coccoidal microfossils such as *Eosphaera tyleri* in the Gunflint Fm (Barghoorn and Tyler, 1965), which have a cell wall thickness of about 100 nm (Brasier et al., 2015). A few discreet occurrences of compartmentalised microfossils composed of apatite and OM occur in the matrix (Fig. 12j, 12k) and are similar to some compartmentalised organic microfossils from the Gunflint Fm, also interpreted to share affinity with *Chroococcus* (e.g. Fig. 8 in Lanier, 1989).

Some Michigamme filaments closely resemble *Gunflintia* microfossils from the Gunflint Fm and occur inside millimeter-size granules of OM and apatite mixed with chert (Fig. 13). Their morphologies, sizes, compositions, and mode of occurrence collectively point to an assignment as filamentous microfossils, possibly as *Gunflintia minuta*. Phosphatic chert from the Michigamme Fm is known to contain pyrite framboids, abundant OM within apatite granules, fossil microbial mat structures, and filamentous apatite structures on the outer coating of some apatite granules, which have been interpreted as microfossils of Fe-oxidising bacteria (Hiatt et al., 2015). In the Paleoproterozoic Zanoega Fm, phosphatic mudstones have layers of apatite concretions that likewise contain tubular filamentous microfossils composed of OM with apatite (Joosu et al., 2015) and some have been interpreted to have formed from sulphur-oxidising bacteria (Lepland et al., 2013). Finally, while a microfossil origin is suspected for the variably patterned networks of OM and apatite in some granules from Michigamme Fm (Fig. 12d-12i), these are more highly degraded and not unambiguously recognizable as microfossils.

In the Biwabik Fm, another taphonomic variety of *Gunflintia* and *Huroniospora* is preserved as dense disseminations of nanoscopic haematite (Barghoorn and Tyler, 1965; Shapiro and Konhauser, 2015). Putative filamentous haematite microfossils can be found inside rare granules from the Biwabik Fm and they have diameters between 0.5 and 4 μm along with lengths of tens to hundreds of microns. Similar filaments previously reported in samples from the Corsica mine of the Biwabik Fm have *Gunflintia*-like filaments with diameters between 1 and 5 μm and composed of fine haematite disseminations in chert (Cloud and Licari, 1968; Shapiro and Konhauser, 2015). Some of the filamentous haematite microfossils in the Biwabik Fm share similarities in size and morphology with modern filamentous Fe-oxidising bacteria in the Franklin seamount of Papua New Guinea (Boyd and Scott, 2001). Such filamentous haematite microfossils are similar to others in the Lake Superior area interpreted to have a biological origin (Leith, 1903; Gruner, 1946; LaBerge, 1967; 1973; Lougheed, 1983, Shapiro and Konhauser, 2015).

Other haematite granules contain spheroids typically around 10 μm composed of disseminated haematite and accessory carbonate and morphologically resemble *Huroniospora* (Fig. 11a, 11b, 11e, 11j). In coarse chert laminations inside stromatolite columns, there are micron-size haematitic coccoidal microfossils that are similar to *Myxococcoides*, smaller but morphologically similar to others preserved in granules. In some haematite granules, there are spheroidal structures with sizes more than 100 μm in diameter (Fig. 11c, 11d), which are composed of haematite and carbonate in chert. These large spheroids are not necessarily microfossils; if they are, many specimens would be larger than the large extant cyanobacterium *Chroococcidiopsis sp*, which are generally smaller than 50 μm. Alternatively, they could be sulphur-oxidising bacteria, akin to *Thiomargarita sp.*, which are known to grow large sizes, sometimes in excess of hundreds of microns, in phosphorites (Schulz and Schulz, 2005; Bailey et al., 2007). Cases have also been made for sulphur-metabolising filamentous microfossils preserved in pyrite in late Paleoproterozoic chert from the Duck Creek Fm (Schopf et al., 2015) and for large-size microfossils in the Neoarchean Gamohaan Fm (Czaja et al., 2016). Lastly, similar to regular network patterns in Michigamme organo-apatite granule, some regular patterns of haematite structures in Biwabik granules might represent highly degraded microfossils (Fig. 8d, 8e), but they might not even be microfossils at all. In brief, the filaments and spheroids in Lake Superior chert are preserved either as degraded OM, an admixture of apatite with finely disseminated OM, and associated detrital-diagenetic sericite-muscovite and anatase-rutile, or as partial replacements with pyrite or haematite. Therefore, there are morphological similarities between *bona fide* filamentous and coccoidal microfossils in granules from late Paleoproterozoic cherts from Lake Superior area and microfossils previously reported, and while these occur in a range of mineral assemblages, some associated specimens are highly degraded.

5.3. Wave action and the diagenetic oxidation of biomass in the formation of granules

Leith (1903) and Gruner (1924, 1946) discussed the “mottled granules” or “spherites” in individual granules from the Biwabik Fm and specifically proposed that they might be microfossils. Later papers (LaBerge, 1973; Lougheed, 1983) summarized and expanded this earlier work on granules and discussed further the biogenicity of BIFs. Millimetric and sub-millimetric granules of concentric, equidistant, and laminated OM in black chert from the Gunflint Fm (Fig. 5e, 5g) have the simplest mineralogy of all granules studied and thus are likely an end-member in terms of preservation. Evidence that some granules formed as primary features in a wave-agitated environment includes 1) their occurrence in a unit just above the Pokegama sandstone, a well-sorted orthoquartzite interpreted as a beach or nearshore deposit, 2) association with broken fragments of algal columns, which suggests significant wave and current action, as well as 3) various sedimentological textures and shapes that can be variably interpreted by wave-action or possible Liesegang effects. The presence of hematite in Biwabik granules can be explained by the dehydration of primary ferrihydrite, while the adsorption of these such nanoscopic phases by microbial mats could have contributed to form granules by wave-action during sedimentation. In addition, the co-occurrence of anatase, rutile, and sericite-muscovite in the Michigamme chert suggest that these are detrital particles and that wave action could also have contributed to the rounding of these granules prior to organic degradation. However, the Biwabik and Michigamme granules also preserve mineralogical and textural evidence for oxidised biomass.

The presence of diagenetic carbonate, apatite, magnetite, and stilpnomelane inside granules, such as those from the Biwabik Fm, requires a corollary to the wave-action model; one that takes into account their overall geochemical-mineralogical compositions. Also, some morphological features of the granules remain unexplained by this model, such as granules with concentric equidistant laminations composed of OM (Fig. 5g), pyrite (Fig. 5e), anatase (Fig. 12o), haematite (Fig. 8g) and magnetite (Fig. 10d). A comprehensive model of granule formation should thus take into account all these independent observations, which we suggest involves *in situ* diagenetic oxidation reactions of OM during putrefaction of microbial biomass and the resulting formation of granules that form fractal patterns akin to those seen in the B-Z reaction (Fig. 1e, 1f).

Organic matter can be oxidised by Fe^{3+} in the absence of biologically-mediated reactions (Amstaetter et al., 2012; Kohler et al., 2013). The non-biological oxidation of OM during diagenesis can occur according to Equations 1 to 4, depending on the availability of electron acceptor compounds:

$$CH_3COOH + 3Fe(OH)_3 \rightarrow 2HCO_3^- + Fe_3O_4 \bullet xH_2O + 2H^+ \quad \text{(Eq. 1)}$$

$$CH_3COOH + SO_4^{2-} \rightarrow 2HCO_3^- + HS^- + H^+ \quad \text{(Eq. 2)}$$

$$CH_3COOH + 4PO_4^{3-} \rightarrow 2HCO_3^- + 4PO_3^{3-} + 2H^+ \qquad \text{(Eq. 3)}$$

$$CH_3COOH + BrO_4^- \rightarrow 2HCO_3^- + Br^- + 2H^+ \qquad \text{(Eq. 4)}$$

In these equations, CH_3COOH is acetic acid taken as a simplification for carboxyl groups in humic acids. Humic acids are essentially alkylated and polyaromatic hydrocarbons with carboxyl, ketone, and alcohol functional groups, and is thus similar to biological OM (Vandenbroucke and Largeau, 2007). This is important because OM with such molecular functional groups can be preserved during the metamorphic maturation of biomass (e.g. Boyce et al., 2002; Bernard et al., 2007; 2009). This background can be used to explore the hypothesis that the concentric equidistant laminated mineral patterns that characterize many cherty, haematitic, phosphatic, clay-rich, and OM-rich granules can be attributed to the preservation of oxidative reaction fronts in chemically-oscillating reactions during diagenesis (Fig. 16).

Organic matter in the Michigamme phosphatic chert has C-XANES spectra that show the residual presence of aliphatic and carboxyl groups (Fig. 4), which have been reported from various other sources of natural carbons (Bernard et al., 2012; Boyce et al., 2002; Cody et al., 1996; De Gregorio et al., 2011; Hitchcock and Ishii, 1987). These functional groups are similar to those from OM in Triassic fossil spores in limestones, which include ketones, phenols, and carboxylic acids (Bernard et al., 2007), and to OM in the Gunflint Fm, which contains phenols and carboxylic acid as well as strong 1s-π^* and 1s-σ^* transitions of polyaromatic carbon (De Gregorio et al., 2009; Moreau and Sharp, 2004). Together with single broad peaks for OM in the centres of diagenetic dolomite rhombs and broad Raman D-bands that encompass several of these functional groups, these characteristics are further consistent with the presence of heteroatoms of O, N, S, and P in acid-insoluble residues from the Gunflint Fm, and thus a biological origin for this OM (De Gregorio et al., 2009). The heteroatom-bearing degraded OM, from the Gunflint and Michigamme formations thus originated from biomass that was degraded and oxidized by both biological and non-biological processes.

In our samples from the Gunflint Fm, we only found evidence for chemically-precipitated minerals such as quartz, carbonate, and pyrite, and hence, this is consistent with the compositions of reactants and products of known chemically-oscillating reactions of oxidising microbial biomass, which can be invoked as a major process for these granules. In comparison, the co-occurrence of anatase, rutile, sericite-muscovite, and disseminations of hematite in both the Michigamme and Biwabik chert suggest that these are detrital particles. Wave action may thus also have contributed to the rounding of the granules prior to organic degradation, but the Biwabik and Michigamme granules also preserve mineralogical evidence for oxidised biomass in the form of rosettes, granules, and concretions, which can be considered fractal patterns as they present similar patterns at various scale dimensions. The mineralogical mode of preservation of granule is thus related to the presence of detrital particles, carboxylic acids, and the availability of oxidants in the diagenetic environment, as suggested in equations 1 to 4.

5.4. Chemically-oscillating reactions in mineralogy, sedimentology, and micropaleontology

In the classical B-Z reaction, carboxylic acids are oxidised with bromate-bromide and sulphate while the reaction products include sulphide, brominated organic molecules, and bicarbonate. In natural environments, other oxidants such as phosphoric acid, ferrihydrite, sulphate, and oxidised halogens must contribute to the oxidation of biomass. The products can then include ^{13}C-depleted bicarbonate that precipitates as various diagenetic carbonate minerals, phosphate with variable oxidation states (e.g. White and Metcalf, 2007) that precipitates as apatite, hydrogen sulphide that readily forms greigite and pyrite, and ferric-ferrous hydrated oxides and silicates that can become diagenetic (and metamorphically-crystallized) magnetite and phyllosilicates. These reaction products then co-exist with the unreactive residue of oxidised biomass, which are polycyclic aromatic hydrocarbons and kerogen that can thermally convert to graphitic carbons. Oxidized wavefronts of OM are proposed here to start from randomly located centres within masses of degrading microbial colonies in silica-saturated waters, expanding centrifugally outward within the chemical sedimentary gel precursor to chert (Fig. 16a). Such non-equilibrium reactions under standard conditions (P = 1atm, T = 298 K; Fig. 1) must be favoured in diagenetic settings in which the limited availability of free water leads to higher (molar) concentrations of oxidants in pore spaces and the production of acid (Eq. 1-4). In the classical B-Z reaction, malonic acid ($C_3H_4O_4$) is oxidised with strong oxidants such as $KBrO_4$, which creates out-of-equilibrium concentric redox fronts that propagate away from oxidising sites over minutes time scales (Fig. 1; Zaikin and Zhabotinsky, 1970; Epstein et al., 1983; Vanag and Epstein 2003). The presence of carboxyl groups in OM from the Gunflint and Michigamme formations shows that key residual reactants from the reactions in equations 1 to 4 are preserved in minerals associated with OM and inside granules.

The mineralised products of the proposed chemically-oscillating reactions include carbonate, pyrite, and ferric-ferrous silicates (e.g. stilpnomelane) and oxides (e.g. magnetite), which are variably found within granules (Fig. 16). Notably, some of these minerals in granule rims can precipitate from reaction products in equations 1 to 4. Characteristic B-Z fractal patterns can thus be recognised as mineralised rims or concentric layers of 1) magnetite, hematite, apatite, and carbonate in the Biwabik chert (Fig. 8h, 9b, 9g), 2) 1) carbonate and pyrite in the Gunflint chert (Fig. 5e, 5i), and 3) apatite, carbonate, graphitic carbon, and anatase in the Michigamme chert (Fig. 12o, 12p-12s, 14g). The systematic occurrence of ^{13}C-depleted carbonate in chert from the Gunflint (Winter and Knauth, 1992), Biwabik (Perry et al., 1973), and Michigamme formations (Tables 3 and 4) points to the oxidation of OM as an important reaction during diagenesis. In brief, the proposed chemically-oscillating reactions during the oxidation of biomass could be mineralised as fractal patterns preserved as laminated concentric and non-intersecting mineral patterns, including granules, rosettes, concretions, and botryoid-type laminations. Botryoids share similarity with B-Z type patterns and, while this observation has never been adopted, botryoids have been previously reported in ferruginous-silicified microbial mats and directly associated with microfossils (e.g. Preston et al., 2011). Hence, key diagenetic minerals occurring as mineralised, rounded, concentric, and/or equidistant layers in granules can be interpreted to represent fractal patterns that repeat at multiple dimension scales, and forming from putrefying microbial biomass.

In phosphatic chert from the shallow-marine Michigamme Fm, apatite granules have millimetre sizes and often contain microfossils composed of OM with apatite or degraded microfossil-like patterns. The precursor phosphate to these mineral assemblages was likely concentrated by micro-organisms that would have included cyanobacteria (Benzerara et al., 2014) or by large sulphur-oxidising bacteria (Schulz and Schulz, 2005). The oxidation of putrefying microbial biomass would have generated HCO_3^- and H^+, lowering alkalinity, and would have triggered diagenetic apatite precipitation. Authigenic apatite forms in pore water solutions under oxic or sub-oxic conditions when fluorapatite supersaturation is achieved (van Cappellen and Berner, 1991; Ruttenberg, 2005). Oxidants such as O_2, ferrihydrite, sulphate, and phosphate can contribute to the non-biological oxidation of microbial OM and to the propagation of redox fronts. Anatase and rutile in Michigamme granules is interpreted to be diagenetic minerals that grew from Ti ions in pore water, most likely from a detrital source (Force, 1991). Submicron-size anatase crystals can form concentric layers that envelope some apatite granules (Fig. 12o) and are interpreted to form patterns from chemically-oscillating reactions. Their size is comparable to anatase crystals a few tens of nanometres in diameter, which are thermodynamically more stable than similarly-sized rutile crystals (Gribb and Banfield, 1997). Besides, TiO_2 crystals are also known to be excellent photocatalysts that help degrade OM (Fujishima and Zhang, 2006), and thus could have contributed to oxidise biomass during the earliest stages of diagenesis. These reactions are thus proposed to produce spheroidally-concentric B-Z type patterns akin to those in Fig. 1e and 1f around microbial colonies during the diagenetic oxidation of their biomass (Fig. 16). Another useful comparison is with apatite granules from the Neoproterozoic Doushantuo phosphorite that contain ubiquitous microfossils and rims with rounded equidistant laminations of apatite and pyrite (She et al., 2014), which could have formed from similar processes. Therefore, the origin of granules involves diagenetic chemically-oscillating reactions as seen from the mineral compositions of rounded, equidistant, and laminated patterns.

Microscopic rosettes are proposed to represent fractals one dimension scale smaller than granules, some of which can be also located between stromatolite columns – for instance in the Jhamarkotra phosphorite (Papineau et al., 2016). Siderite rosettes are known to form during diagenetic to low grade metamorphic conditions (at T = 170^{o}C and P = 1.2 kbar) in experiments where glucose is oxidised by ferrihydrite to produce siderite (Kohler et al., 2013). Other long-term experiments at room temperature with phosphate and bacteria have further shown that rosettes can develop as individual radially fibrous apatite spheroids, which sometimes forms pairs as dumbbell-shaped structures (Blake et al., 1998). Rosettes with apatite have been reported to occur in a number of rocks, including: 1) in Lower Cambrian and Neoproterozoic phosphorites from China associated with chert and framboidal pyrite (Sun et al., 2014), 2) in the intercolumnar space of stromatolitic phosphorite in late Paleoproterozoic Aravalli Supergroup in India where they also contain carbonate inclusions in apatite and cores of chert (Papineau et al., 2016), 3) in organic-rich chert of the late Paleoproterozoic FB Fm in the Francevillian Supergroup in Gabon where they occur as apatite cores surrounded by quartz and embedded in a matrix of siderite and stilpnomelane (Mossman et al., 2005), and 4) in the Gunflint iron formation where they are composed of siderite, apatite, and haematite or only of siderite or haematite with chert (LaBerge, 1973; Lougheed et al., 1983; Heaney and Veblen, 1991; Carrigan and Cameron, 1991). Many hypotheses have been proposed for the origin of rosettes including fossil cyanobacteria (LaBerge, 1973; Awramik and Barghoorn, 1977; Chauhan, 1979), fossil eukaryotic organisms (Kazmierczak, 1979), structures that crystallize from viscous and impure silica gels (Oehler, 1976), and as early diagenetic structures (Carrigan and Cameron, 1991; Papineau et al., 2016). In light of our new data, the mineral compositions, and the concentric nature of rosettes shows consistency with a similar mechanism to that invoked for granules: chemically-oscillating reactions during the early diagenetic oxidation of microbial biomass (Fig. 16; Papineau et al., 2016).

6. Conclusions

While some granules have a detrital-accretionary origin, for instance when they are composed of detrital phase like clays, titanium dioxide, or hematite, but our new observations suggest that both biological and diagenetic processes were also involved in their formation. The occurrence of ^{13}C-depleted carbonate in the Michigamme, Gunflint, and Biwabik formations suggests the oxidation of OM into carbonate. The common co-occurrence of pyrite in these cherts suggest the oxidation of OM during diagenesis in the presence of sulphate. Some highly depleted $\delta^{13}C_{org}$ values down to -46‰ in the Michigamme Fm, suggest transient episodes of methane cycling, possibly associated with anaerobic and aerobic microenvironments.

We report new observations of mineral patterns akin to the characteristic fractal patterns from the classical B-Z reaction (Fig. 1) and suggest that these are fractal patterns that form micrometre-size rosettes, millimetre-size granules, to centimetre-plus size of concretions (Table 4). While the morphologies of life forms are often characterised by fractal patterns (e.g. dendrite, stripes, veins) powered in part by the metabolism of carboxylic acids (e.g. the tri-carboxylic acid cycle), other fractal patterns continue to be produced during the putrefaction of biomass and the oxidation of carboxylic acids. Detailed petrographic, mineralogical, and sedimentological documentation of granules in Lake Superior cherts reveals the occasional occurrence of putative microfossils, diagenetic minerals, as well as repeating patterns made of precipitated minerals (quartz, apatite, carbonate, magnetite, ferric-ferrous phylosilicates). In particular, the presence of carboxyl groups in OM from the Gunflint and Michigamme cherts shows the preservation of residual reactants. Products of B-Z type reactions include precursor molecules to ^{13}C-depleted carbonate, as well as pyrite, apatite, and ferric-ferrous silicates (e.g. stilpnomelane, greenalite, vermiculite) and oxides (e.g. magnetite), all of which are considered diagenetic minerals when they occur in granules, most clearly when they have rounded, equidistant, and finely laminated concentric layers. Chemically-oscillating reactions are proposed to significantly contribute to the formation of diagenetic spheroids such as rosettes, granules, and concretions, all of which share similarities with B-Z type fractal patterns, in particular regarding the fact that they preserve similar mineral patterns of concentric equidistant laminations at several dimension scales. We further suggest that the origin of rosettes of muscovite, haematite, apatite, and pyrite are due to such processes during early diagenesis. Under standard conditions, concentric patterns made of reaction products would expand outward through an EPS-silica gel, possibly through liesegang-type diffusion, forming layers of OM mixed with oxidised (e.g. phosphate and carbonate) or reduced products (e.g. pyrite and ferric-ferrous minerals). Authigenic apatite occurs as granules and is usually associated with OM, which often preserves microfossil morphologies or patterned networks. Pyrite or haematite can also replace OM in microfossils, and anatase and rutile occur as diagenetic phases associated with concentric rims or among microfossils. The proposed chemically-oscillating reactions likely significantly contribute to the preservation and degradation of microfossils, analogously to animal and plant fossils being often present in concretions. We conclude that these late Paleoproterozoic microfossils from the Lake Superior area were variably preserved because of the local and pore water abundances of ferrihydrite, phosphate, sulphate, oxygen, and other oxidants (i.e. possibly bromate).

Future work will investigate trace bromine and sulphate concentrations in accessory minerals. Additionally, experiments utilising naturally-occurring microbial remains and various siliceous gels containing ferric iron or phosphate need to investigate the range of possible reactants and concentrations for chemically-oscillating reactions under standard or diagenetic conditions. This new theory of putrefaction after the GOE, suggests that diagenetic spheroids should be more abundant in late Palaeoproterozoic rocks and predicts that these processes and objects should not be restricted to the Lake Superior area and may occur worldwide in contemporary rocks. Diagenetic spheroids can thus be regarded as mineral fractal patterns precipitated from chemically-oscillating reactions, which creates characteristic patterns around decaying dead organisms, over several scale dimensions.

Our new model provides many new hypotheses to test: 1) B-Z type processes can produce rosettes and granules in cherts and phosphorites which should contain diagenetic carbonate and phosphate minerals, 2) microfossil remains of OM in chert should be preserved, perhaps rarely, in granules including in Paleoarchean cherts (e.g. Schopf and Kudryavtsev, 2012), 3) jaspers with concretions and granules should occasionally contain haematitic microfossils, and since the Eoarchean (Dodd et al., 2017), and 4) phosphate-rich rocks may contain metabolically-diverse microbial ecosystems variably-preserved in apatite concretions, granules, and rosettes. Notably, microfossils are often concentrated within granules and associated with a range of diagenetic mineral products, which represents a robust petrologic context to conclude on the biological origin of candidate microfossils and thus a promising model to resolve past controversies on their biogenecity. These conclusions and predictions are thus highly relevant to the debates on evidence of Paleoarchean and Eoarchean life, and they augment the repertoire of biosignatures to search for fossil extraterrestrial life.

7. Acknowledgements

DP acknowledges financial support from the London Centre for Nanotechnology, University College London, Carnegie Institution for Science, NASA Astrobiology Institute (grant # NNA04CC09A), the NASA Exobiology and Evolutionary Biology Program (grant # NNX08AO16G), NASA Early Career Fellowship Program, Carnegie of Canada, and the W.M. Keck Foundation. ZS acknowledges financial support from National Natural Science Foundation of China (grant # 41272038) and State Key Laboratory of Biogeology and Environmental Geology, China University of Geosciences (grant # GBL11610). DP also thanks Melanie Humphrey for access to drill cores, W. Cannon for advice on outcrop location and access, Ahmed Aibak for assistance in the field and core library, Philip Fralick, Richard Ojakangas, and Hiroshi Ohmoto for organising field trips to some of the visited localities, and S. Mojzsis for providing Gunflint sample *GF-7*. STXM data was acquired at the Advanced Light Source, which is supported by the Director, Office of Science, Office of Basic Energy Sciences, of the U.S. Department of Energy (under Contract No. DE-AC02-05CH11231) and David D.A. Kilcoyne is thank for assistance with these analyses. Constructive criticism by Marc Norman, Paul Strother, Bevan French, and two anonymous reviewers contributed to improve this manuscript.

8. References

Alexander, C.M.O'D., Fogel, M., Yabuta, H., and Cody, G.D. (2007) The origin and evolution of chondrites recorded in the elemental and isotopic compositions of their macromolecular organic matter. *Geochimica et Cosmochimica Acta* **71,** 4380–4403.

Alléon, J., Bernard, S., Le Guillou, C., Marin-Carbonne, J., Pont, S., Beyssac, O., McKeegan, K., and Robert, F. (2016) Molecular preservation of 1.88 Ga Gunflint organic microfossils as a function of temperature and mineralogy. *Nature Communications*, DOI: 10.1038/ncomms11977.

Amstaetter, K., Borch, T., and Kappler, A. (2012) Influence of humic acid imposed changes of ferrihydrite aggregation on microbial Fe(III) reduction. *Geochimica et Cosmochimica Acta* **85,** 326-341.

Awramik, S.M. and Barghoorn, E.S. (1977) The Gunflint microbiota. *Precambrian Research* **5,** 121-142.

Bailey, J.V., Joye, S.B., Kalanetra, K.M., Flood, B.E. and Corsetti, F.A. (2007) Evidence of giant sulphur bacteria in Neoproterozoic phosphorites. *Nature* **445,** 198-201.

Barge, L.M., Cardoso, S.S.S., Cartwright, J.H.E., Doloboff, I.J., Flores, E., Macias-Sanchez, E., Sainz-Diaz, C. I., and Sobron, P. (2016) Self-assembling iron oxyhydroxide/oxide tubular structures.: laboratory-grown and field examples from Rio Tinto. Proc. R. Soc. A **472,** 20160466, 1-19.

Barghoorn, E.S. and Tyler, S.A. (1965) Microorganisms from the Gunflint Chert. *Science* **147,** 563-577.

Bentor, Y.K. (1980) Phosphorites - The unresovled problems. *SEPM Special Publication No. 29, 3-18.*

Benzerrara, K., Skouri-Panet, F., Li, Ferard, C., Gugger, M., Laurent, T., Couradeau, E., Ragon, M., Cosmidis, J., Menguy, N., Margaret-Oliver, I., Tavera, R., Lopez-Garcia, P., and Moreira, D. (2014) Intracellular Ca-carbonate biomineralization is widespread in cyanobacteria. *P.N.A.S.* **111**, 10933-10938.

Bernard, S., Wirth, R., Schreiber, A., Schulz, H.-M., and Horsfield, B. (2012) Formation of nanoporous pyrobitumen residues during maturation of the Barnett Shale (Fort Worth Basin). *International Journal of Coal Geology* **103**, 3-11.

Bernard, S., Benzerara, K., Beyssac, O., Brown, G.E., Grauvogel Stamm, L., and Duringer, P. (2009) Ultrastructural and chemical study of modern and fossil sporoderms by Scanning Transmission Y-ray Microscopy (STXM). *Review of Palaeobotany and Palynology* **156,** 248-261.

Bernard, S., Benzerara, K., Beyssac, O., Menguy, N., Guyot, F., Brown, G.E., and Goffe, B. (2007) Exceptional preservation of fossil plant spores in high-pressure metamorphic rocks. *Earth and Planetary Science Letters* **262,** 257-272.

Beyssac, O., Goffe, B., Chopin, C., and Rouzaud, J.N. (2002) Raman spectra of carbonaceous material in metasediments: a new geothermometer, *J. Met. Geol.* **20,** 859– 871

Blake, R.E. O'Neil, J.R., and Garcia, G.A. (1998) Effects of microbial activity on the $\delta^{18}O$ of dissolved inorganic phosphate and textural feature of synthetic apatites. *American Mineralogist* **83,** 1516-1531.

Boyce, C.K., Cody, G.D., Feser, M. (2002) Organic chemical differentiation within fossil plant cell walls detected with X-ray spectromicroscopy. *Geology* **30**, 1039–1042.

Boyd, T.D. and Scott, S.D. (2001) Microbial and hydrothermal aspects of ferric oxyhydroxides and ferrosic hydroxides: the example of Franklin Seamount, Western Woodlark Basin, Papua New Guinea. *Geochemical Transactions* **2**, 45, doi:10.1039/b105277m.

Brasier, M.D., Antcliffe, J., Saunders, M., and Wacey, D. (2015) Changing the picture of Earth's earliest fossils (3.5-1.9 Ga) with new approaches and new discoveries. *P. N. A. S.* **112,** 4859-4864.

Brehm, U., Krumbein, W.E., and Palinska, K.A. (2003) Microbial spheres: a novel cyanobacterial-diatom symbiosis. *Naturwissenschaften* **90,** 136-140.

Buick, R. (1992) The antiquity of oxygenic photosynthesis: evidence from stromatolites in sulphate-deficient Archean lakes. *Science* **255,** 74-77.

Carrigan, W.J. and Cameron, E.M. (1991) Petrological and stable isotope studies of carbonate and sulfide minerals from the Gunflint Formation, Ontario: evidence for the origin of early Proterozoic iron-formation. *Precambrian Research* **52,** 347-380.

Chauhan, D.S. (1979) Phosphate-bearing stromatolites of the Precambrian Aravalli phosphorite deposits of the Udaipur region, their environmental significance and genesis of phosphorite. *Precambrian Research* **8,** 95-126.

Cloud, P.E. and Licari, G.R. (1968) Microbiotas of the banded iron formations. *P. N. A. S.* **61,** 779-786.

Cody, G.D., Heying, E., Alexander, C.M.O'D., Nittler, L.R., Kilcoyne, A.L.D., Sandford, S.A., and Stroud, R.M. (2011) Establishing a molecular relationship between chondritic and cometary organic solids. *Proceedings of the National Academy of Sciences* **108**, 19171-19176.

Cody, G.D., Botto, R.E., Ade, H., and Wirick, S. (1996) The application of soft X-ray microscopy to the in-situ analysis of sporinite in coal. *International Journal of Coal Geology* **32**, 69-86.

Crosby, C.H., Bailey, J., and Sharma, M. (2014) Fossil evidence of iron-oxidizing chemolithotrophy linked to phosphogenesis in the wake of the Great Oxidation Event. *Geology* **42,** 1015-1018.

Czaja, A.D., Beukes, N.J., and Osterhout, J.T. (2016) Sulfur-oxidising bacteria prior to the Great Oxidation Event from the 2.52 Ga Gamohaan Formation of South Africa. *Geology* **44,** 983-986.

De Gregorio, B.T., Sharp, T.G., Flynn, G.J., Wirick, S., and Hervig, R.L. (2009) A biogenic origin for Earth's oldest putative microfossils. *Geology* **37**, 631-634.

De Gregorio, B.T., Sharp, T.G., Rushdi, A.I., and Simoneit, B.R.T. (2011) Bugs or gunk? Nanoscale methods for assessing the biogenicity of ancient microfossils and organic matter. In: Golding, S.D., Glikson, M. (Eds.), *Earliest Life on Earth: Habitats, Environments, and Methods of Detection*, Springer, Dordrecht, Netherlands, 239-289.

Desmarais, D. (2001) Isotopic evolution of the biogeochemical carbon cycle during the Precambrian. *Reviews in Mineralogy and Geochemistry* **43**, 555-578.

Dodd, M.S., Papineau, D., Grenne, T., Slack, J.F., Rittner, M., Pirajno, F., O'Neil, J., and Little, C.T.S. (2017) Evidence for early life in Earth's oldest hydrothermal vent precipitates. *Nature* **543,** 60-64, *DOI* 10.1038/nature21377.

Eigenbrode, J.L. and Freeman, K.H. (2006) Late Archean rise of aerobic microbial ecosystems. P.N.A.S. 103, 15759-15764.

Epstein, I.R. Kustin, K., De Kepper, P., and Orban, M. (1983) Oscillating Chemical Reactions. *Scientific American*, 112-123.

Force, E.R. (1991) Geology of Titanium-Mineral Deposits. *Geol. Soc. Am. Sp. Pap.* **259,** 112pp.

Fralick, P., Davis, D., and Kissin, S.A. (2002) The age of the Gunflint Formation, Ontario, Canada: single zircon U-Pb age determinations from reworked volcanic ash. *Canadian Journal of Earth Sciences* **39,** 1085-1091.

French, B.M. (1968) Progressive contact metamorphism of the Biwabik Iron-Formation Mesabi Range, Minnesota. *Minnesota Geological Survey Bulletin* **49,** 103 p.

Fujishima, A. and Zhang, X. (2006) Titanium dioxide photocatalysis: present situation and future approaches. *Comptes Rendus de Chimie* **9,** 750-760.

Garcia-Ruiz, J.M., Nakouzi, E., Kotopoulou, E., Tamborrino, L., and Steinbock, O. (2017) Biomimetic mineral self-organization from silica-rich spring waters. *Science Advances* **3,** e1602285, 1-6.

Gribb, A.A., and Banfield, J.F. (1997) Particle size effects on transformation kinetics and phase stability in nanocrystalline TiO_2. *Am. Mineral.* **82,** 717-728.

Gruner, J.W. (1924) Contributions to the geology of the Mesabi Range, Minnesota. *Minnesota Geological Survey Bulletin* **19**, 71 p.

Gruner, J.W. (1946) Mineralogy and geology of the Mesabi Range. St. Paul, MN, Office of the Commissional of the Iron Range Resources and Rehabilitaton, 127 p.

Hayes, J.M. (1994) Global methanotrophy at the Archean-Proterozoic transition, In: Bengtson S. (Ed.) *Nobel Symposium 84, Early life on Earth*. Columbia University Press, New York, p. 220-236

Heaman, L.M., Easton, R.M., Hart, T.R., Hollings, P., MacDonald, C.A., and Smyk, M., (2007) Further refinement of the timing of Mesoproterozoic magmatism, Lake Nipigon region, Ontario. *Canadian Journal of Earth Sciences* **44,** 1055–1086.

Heaney, P.J. and Veblen, D.R. (1991) An examination of spherulitic dubiomicrofossils in Precambrian banded iron formations using the transmission electron microscope. *Precambrian Research* **49,** 355-372.

Heimann, A., Johnson, C.M., Beard, B.L., Valley, J.W., Roden, E.E., Spicuzza, M.J., and Beukes, N.J. (2010) Fe, C, and O isotope compositions of banded iron formation carbonates demonstrate a major role for dissimilatory iron reduction in 2.5Ga marine environments. *Earth and Planetary Science Letters* **294,** 8-18.

Hiatt, E.E., Pufahl, P.K., and Edwards, C.T. (2015) Sedimentary and associated fossil bacteria in a Paleoproterozoic tidal flat in the 1.85 Ga Michigamme Formation, Michigan, USA. *Sedimentary Geology* **319,** 24-39.

Hitchcock, A.P., and Ishii, I. (1987) Carbon K-shell excitation spectra of linear and branched alkanes. *J. Electron Spectrosc. Relat. Phenomena* **42,** 11–26.

Hitchcock, A.P. and Biron, C.E. (1980) Inner-shell excitation of formaldehyde, acetaldehyde, and acetone studied by electron impact. *Journal of Electron Spectroscopy and Related Phenomena* **19,** 231-250.

Hofmann, H.J. (1972) Stromatolites: characteristics and utility. *Earth Sciences Reviews* **9,** 339-373.

House, C.H., Schopf, J.W., and Stetter, K.O. (2003) Carbon isotopic fractionation by Archaeans and other thermophilic prokaryotes. *Organic Geochemistry* **34,** 345-356.

House, C.H., Schopf, J. W., McKeegan, K.D., Coath, C.D., Harrison, T.M., Stetter, K.O. (2000) Carbon isotopic composition of individual Precambrian microfossils. *Geology* **28,** 707-710.

Igisu, M., Ueno, Y., Shimojima, M., Nakashima, S., Awramik, S.M. Ohta, H., Maruyama. (2009) Micro-FTIR spectroscopic signature of bacterial lipids in Proterozoic microfossils. *Precambrian Research* **173,** 19-26.

Joosu, L., Lepland, A., Kirsimae, K., Romashkin, A.E., Roberts, N.M.W., Martin, A.P., and Crne, A. (2015) The REE-composition and petrography of apatite in 2 Ga Zaonega Formation, Russia: The environmental setting for phosphogenesis. *Chemical Geology* **395,** 88-107.

Juniper, S. K. & Fouquet, Y. Filamentous iron-silica deposits from modern and ancient hydrothermal sites. *Canadian Mineralogist* **26**, 859-869 (1988).

Karhu, J.A. and Holland, H.D. (1996) Carbon isotopes and the rise of atmospheric oxygen. *Geology* **24**, 867-870.

Karkhanis, S. N. (1976) Fossil iron bacteria may be preserved in Precambrian ferroan carbonate. Nature **261,** 406-407.

Kazmierczak, J. (1979) The Eukaryotic nature of Eosphaera-like ferriferous structures from the Precambrian Gunflint iron formation, Canada: A comparative study. *Precambrian Research* **9,** 1-22.

Kilcoyne, A. L. D., Tyliszczak, T., Steele, W. F., Fakra, S., Hitchcock, P., Franck, K., Anderson, E., Harteneck, B., Rightor, E. G., Mitchell, G. E., Hitchcock, A. P., Yang, L., Warwick, T., Ade, H. (2003). Interferometer-controlled scanning transmission X-ray microscopes at the Advanced Light Source, *The Journal of Synchrotron Radiation* **10,** 125-136.

Knoll, A.H. and Simonson, B. (1981) Early Proterozoic microfossils and penecontemporaneous quartz cementation in the Sokoman Iron Formation, Canada. *Science* **211,** 478-480.

Knoll, A.H. and Barghoorn, E.S. (1975) Precambrian Eukaryote organisms: a reassessment of the evidence. *Science* **190,** 52-54.

Köhler, I., Konhauser, K.O., Papineau, D., Bekker, A., and Kappler, A. (2013) Biological carbon precursor to diagenetic siderite spherulites in banded iron formations. *Nature Communication* **4**:1741, 1-7.

Kouketsu, Y., Mizykami, T., Mori, H., Endo, S., Aoya, M., Hara, H., Nakamura, D., and Wallis, S., (2014) A new approach to develop the Raman carbonaceous material geothermometer for low-grade metamorphism using peak width. *Island Arc* **23,** 33-50.

LaBerge, G.L. (1973) Possible biological origin of Precambrian Iron-Formations. *Economic Geology* **68,** 1098-1109.

LaBerge, G.L. (1967) Microfossils and Precambrian Iron-Formations. *G.S.A. Bull.* **78,** 331-342.

Lafhid, A., Beyssac, O., Deville, E., Negro, F., Chopin, C., and Goffe, B. (2010) Evolution of the Raman spectrum of carbonaceous material in low-grade metasediments of the Glarus Alps (Switzerland). *Terra Nova* **22,** 354-360.

Lanier, W.P. (1989) Interstitial and peloid microfossils from the 2.0 Ga Gunflint Formation: Implications for the Paleoecology of the Gunflint stromatolites. *Precambrian Research* **45,** 291-318.

Leith, C.K., (1903) The Mesabi iron-bearing district of Minnesota. *U.S, Geological Survey Monograph* **43***,* 316 pp.

Lepland, A., Joosu, L., Kirsimäe, K., Prave, A.R., Romashkkin, A.E., Crne, A., Martin, A.P., Fallick, A.E., Somelar, P., Üpraus, K., Mänd, K., Roberts, N.M.W., van Zuilen, M.A., Wirth, R., Schreiber, A. (2013) Potential influence of Sulphur bacteria on Palaeoproterozoic phosphogenesis. *Nature Geoscience*, DOI: 10.1038/NGEO2005.

Little, C. T. S., Glynn, S. E. J. & Mills, R. A. (2004) Four-hundred-and-ninety-million-year record of bacteriogenic iron oxide precipitation at sea-floor hydrothermal vents. Geomicrobiol. J. **21,** 415–429.

Lougheed, M.S. (1983) Origin of Precambrian iron-formation in the Lake Superior region. *G.S.A. Bulletin* **94,** 325-340.

Maliva, R.G., Knoll, A.H., and Simonson, B.M. (2005) Secular change in the Precambrian silica cycle: insights from chert petrology. *GSA Bulletin* **117,** 835-845.

Marshall, C.P., Emry, J.R., and Olcott Marshall, A. (2011) Haematite pseudomicrofossils present in the 3.5-billion-year-old Apex chert. *Nature Geoscience* DOI: 10.1038/NGEO1084.

Marshall, C.P. and Olcott Marshall, A. (2013) Raman hyperspectral imaging of microfossils: potential pitfalls. *Astrobiology* **13,** DOI: 10.1089/ast.2013.1034.

Moreau, J.W. and Sharp, T.G. (2004) A transmission electron microscopy study of silica and kerogen biosignatures in ~1.9 Ga Gunflint microfossils. *Astrobiology* **4,** 196-210.

Mossman, D.J., Gauthier-Lafaye, F., and Jackson, S.E. (2005) Black shales, organic matter, ore genesis and hydrocarbon generation in the Paleoproterozoic Franceville Series, Gabon. *Precambrian Research* **137,** 253-272.

Nelson, G.J., Pufahl, P.K., and Hiatt, E.E. (2010) Palaeoproterozoic constraints on Precambrian phosphorite accumulation, Baraga Group, Michigan, USA. *Sedimentary Geology* **226,** 9-21.

Oehler, D.Z. (1976) Transmission electron microscopy of organic microfossils from the late Precambrian Bitter Springs Formation of Australia: techniques and survey of preserved ultrastructure. *Journal of Paleontology* **50,** 90-106.

Ojakangas, R.W., Marmo, J.S., and Heiskanen, K.I. (2001) Basin evolution of the Paleoproterozoic Karelian Supergroup of the Fennoscandian (Baltic) Shield. *Sedimentology Geology* **141-142,** 255-285.

Pacton, M., Ariztegui, D., Wacey, D., Kilburn, M.R., Rollion-Bard, C., Farah, R., and Vasconcelos, C. (2012) Going nano: a new step toward understanding the processes governing freshwater ooid formation. *Geology* **40,** 547-550.

Papineau, D., De Gregorio, B.T., Fearn, S., Kilcoyne, D., Purohit, R., and Fogel, M.L. (2016) Nanoscale petrographic and geochemical insights on the origin of Paleoproterozoic stromatolitic phosphorites from Aravalli, India. *Geobiology,* DOI 10.1111/gbi12164. 1-30

Papineau, D., Purohit, R., Fogel, M.L., and Shields, G.A. (2013) High phosphate availability as a possible cause for massive cyanobacterial production of oxygen in the Proterozoic atmosphere. *Earth and Planetary Science Letters* **362,** 225-236.

Papineau, D., DeGregorio, B.T., Cody, G.D., O'Neil, J., Steele, A., Stroud, R.M., and Fogel, M.L. (2011) Young poorly crystalline graphite in the >3.8 Gyr old Nuvvuagittuq banded iron formation, *Nature Geoscience* **4,** 376-379.

Papineau, D. (2010) Global biogeochemical changes at both ends of the Proterozoic: Insights from phosphorites, *Astrobiology* **10,** 1-17.

Papineau, D., Mojzsis, S.J., Coath, C.D., Karhu, J.A. and McKeegan, K.D. (2005) Multiple sulfur isotopes of sulfide from sediments in the aftermath of Paleoproterozoic glaciations. *Geochim. Cosmochim. Acta* **69,** 5033-5060.

Rasmussen, B., Fletcher, I.R., Bekker, A., Muhling, J.R., Gregory, C.J., and Thorne, A.M. (2012) Deposition of 1,88-billion-year-old iron formations as a consequence of rapid crustal growth. *Nature* **484,** 498-501.

Ruttenberg, K.C. (2005) The global phosphorus cycle. In: Treatise on Geochemistry, Elsevier, ISBN: 0-08-0443-43-5, pp 585-643.

Schidlowski, M. (2001) Carbon isotopes as biogeochemical recorders of life over 3.8 Ga of Earth history: Evolution of a concept. *Precambrian Research* **106**, 117-134.

Schneider, D.A, Bickford, M.E., Cannon, W.F., Schulz, K.J., and Hamilton, M.A. (2002) Age of volcanic rocks and syndepositional iron formations, Marquette Range Supergroup: implications for the tectonic setting of Paleoproterozoic iron formations of the Lake Superior region. *Can. J. Earth Sci.* **39,** 999-1012.

Schopf , J.W., Kudryavtsev, A.B., Walter, M.R., van Kranendonk, M.J., Williford, K.H., Kozdon, R., Valley, J., Gallardo, V.A., Espinoza, C., and Flannery, D.T. (2015) Sulfur-cycling fossil bacteria from the 1.8-Ga Duck Creek Formation provide promising evidence of evolution's null hypothesis. *P.N.A.S.* DOI: 10.1073/pnas.1419241112.

Schopf, J.W. and Kudryavtsev, A.B. (2012) Biogenecity of Earth's earliest fossils: A resolution of the controversy. *Gondwana Research* **22,** 761-771.

Schopf, J.W., Kudryavtsev, A.B., Agresti, D.G., Czaja, A.D., and Wdowiak, T.J. (2006) Raman imagery: a new approach to assess the chemical maturity and biogenicity of permineralized Precambrian fossils. *Astrobiology* **5,** 333-371.

Schopf, J.W. (1993) Microfossils of the Early Archean Apex Chert: Evidence of the antiquity of life. *Science* **260,** 640-646.

Schulz, H.N. and Schulz, H.D. (2005) Large sulfur bacteria and the formation of phosphorite. *Science* **307,** 416-418.

Schulz, K.J. and Cannon, W.F. (2007) The Penokean orogeny in the Lake Superior region. *Precambrian Research* **157,** 4-25.

Shapiro, R.S. and Konhauser, K.O. (2015) Haematite-coated microfossils: primary ecological fingerprint or taphonomic oddity of the Paleoproterozoic? *Geobiology* **13,** 209-224.

She, Z., Strother, P., and Papineau, D. (2014) Terminal Proterozoic cyanobacterial blooms and phosphogenesis documented by the Doushantuo granular phosphorites II: petrology and carbon isotopes. *Precambrian Research* **251,** 62-79.

She, Z., Strother, P., McMahon, G., Nittler, L.R., Wang, J., Zhang, J., Longkang, S., Ma, C., and Papineau, D. (2013) Terminal Proterozoic cyanobacterial blooms and phosphogenesis documented by the Doushantuo granular phosphorites I: *In situ* micro-analyses of textures and composition. *Precambrian Research* **235,** 20-35.

Simonson, B.M. (1985) Sedimentology of cherts in the Early Proterozoic Wishart Formation, Quebec-Newfoundland, Canada. *Sedimentology* **32,** 23-40.

Sommers, M.G., Awramik, S.M., and Woo, K.S. (2000) Evidence for initial calcite-aragonite composition of lower algal chert member ooids and stromatolites, Paleoproterozoic Gunflint Formation, Ontario, Canada. *Canadian Journal of Earth Sciences* **37,** 1229-1243.

Strauss, H. and Moore, T. B. (1992) Abundances and isotopic compositions of carbon and sulfur species in whole rock and kerogen samples. In *The Proterozoic Biosphere, a* *multidisciplinary study* (eds. J. W. Schopf and C. Klein). Cambridge Univ. Press, Cambridge, pp. 709-798.

Sun, S., Chan, L.S., Y.L. Li (2014) Flower-like apatite recording microbial processes through deep geological time and its implication to the search for mineral records of life on Mars. *American Mineralogist* **99,** 2116-2125.

Tyler, S.A. and Barghoorn, E.S. (1954) Occurrences of structurally preserved plants in pre-Cambrian rocks of the Canadian Shield. *Science* **119,** 606-609

Van Cappellen, P. and Berner, R.A. (1991) Fluorapatite crystal growth from modified seawater solutions, *Geochimica et Cosmochimica Acta* **55,** 1219-1234.

Vanag, V. and Epstein, I.R. (2003) Segmented spiral waves in a reaction-diffusion system. *P.N.A.S.* **25,** 14635-14638.

Vandenbroucke, M. and Largeau, C. (2007) Kerogen origin, evolution and structure. *Organic Geochemistry* **38,** 719-833.

Van Wyck, N. and Johnson, C.M. (1997) Common lead, Sm-Nd, and U-Pb constraints on petrogenesis, crustal architecture and tectonic setting of the Penokean orogeny (Paleoproterozoic) in Wisconsin. *GSA Bulletin* **109,** 799-808.

Wacey, D., Menon, S., Green, L., Gerstmann, D., Kong, C., McLoughlin, N., Saunders, M., and Brasier, M. (2012) Taphonomy of very ancient microfossils from the 3400Ma Strelley Pool Formation and 1900 Ma Gunflint Formation: New insights using a focused ion beam. *Precambrian Research* **220-221,** 234-

Wacey, D., McLoughlin, N., Kilburn, M.R., Saunders, M., Cliff, J.B., and Kong, C. (2013) Nanoscale analysis of pyritised microfossils reveals differential heterotrophic consumption in the ~1.9 Ga Gunflint chert. *P. N. A. S.* **110,** 8020-8024.

White, A.K. and Metcalf, W.W. (2007) Microbial metabolism of reduced phosphorus compounds. *Annual Reviews of Microbiology* **61,** 379-400.

Williford, K.H., Ushikubo, T., Schopf, J.W., Lepot, K., Kitajima, K., and Valley, J.W. (2013)

Preservation and detection of microstructural and taxonomic correlations in the carbon isotopic compositions of individual Precambrian microfossils. *Geochimica et Cosmochimica Acta* **104,** 165-182.

Winter, B.L. and Knauth, L.P. (1992) Stable isotope geochemistry of cherts and carbonates from the 2.0 Ga Gunflint iron formation: implications for the depositional setting, and the effects of diagenesis and metamorphism. *Precambrian Research* **59,** 283-313.

Zaikin, A.N. and Zhabotinsky, A.M. (1970) Concentration wave propagation in two-dimensional liquid-phase self-oscillating system. *Nature* **225,** 535-537.

Tables

- **Table 1:** Stable isotope data of rocks from MMTU drill core from Michigamme Fm.
- **Table 2:** Energy Dispersive Spectroscopy-based compositional analyses of selected minerals in the Michigamme and Biwabik Formations.
- **Table 3:** Stable isotope data of rocks from MMTU drill core (Michigan Technical University).
- **Table 4:** Summary table of the main new observations for the three types of chert studied in this work.

Table 1: Raman band parameters for best fit with linear combinations of Lorentz functions.

Lorentz-fitted parameters	**GF-7 coccoidal microfossil**	**GF-7 filamentous microfossil**	**ME-B1 large coccoids**	**MaryEllen-1 coccoid granule**	**MA0708 coccoidal microfossil**	**MA0708 filamentous microfossil**
G pos	1590	1590	1575	1595	1586	1587
G fwhm	43	43	60	60	33	39
G area	2000	2250	2900	1800	2400	7900
D1 pos	1340	1342	1346	1337	1352	1349
D1 FWHM	95	130	120	110	37	44
D1 area	17000	18000	5000	4500	3200	14700
D2 pos	1615	1615	1620	1620	1620	1620
D2 FWHM	40	40	40	35	25	25
D2 area	8200	7000	580	600	350	1500
D3 pos	1510	1510	1510	1510		
D3 FWHM	200	100	135	135		
D3 area	6500	2200	2200	1200		
D4 pos	1245	1245	1245	1245		
D4 FWHM	160	100	160	150		
D4 area	7000	3500	2200	900		
D5 pos			1450	1450		
D5 FWHM			100	100		
D5 area			450	500		
Temperature Lafhid RA1	267	346	229	280		
Temparture Beyssac	243	245	359	323	387	352
Temperature Kuketsu	274	199	220	242	398	383
average of estimates	261	263	269	282	393	367
1 sigma	16	75	78	41	8	23

Temperature estimates are calculated according to calibrated geothermometres from Beyssac et al. (2002), Lafhid et al. (2010), and Kouketsu et al. (2015). Note that the Beyssac thermometer was not calibrated for crystallization temperatures below 350°C.

Table 2: Carbonates analyses by EDS in ME-B1 and of phosphates analysed by WDS in MA0708

Targets	ME-B1	ME-B1	ME-B1	MA0708	MA0708	MA0708	MA0708
Wt.(%)	**spot 1a**	**spot 2a**	**spot 3a**	**spot 1f**	**spot 1h**	**spot 1l**	**spot 3a**
C K	12.0	4.4	4.9				
O K	36.9	19.8	19.4	39.7	39.9	39.5	39.5
P K		9.9	10.3	18.0	18.2	17.8	17.8
Mg K	1.4						
Ca K	2.6			39.0	39.0	39.4	39.4
Si K	1.7	3.5	2.0	0.1	0.0	0.1	0.0
F K	5.6			3.9	3.5	4.1	4.0
Mn K	21.0						
Fe K	18.8	6.5	3.6				
Ni K		4.8	5.7				
La L		12.3	14.9				
Ce L		20.6	22.3		0.2	0.1	0.1
Nd L		9.2	7.9				
Sm L		4.3	4.6				
Gd L		4.8	4.4				
Y L					0.1		0.1
Totals	100.0	100.1	100.0	100.7	100.8	100.9	101.0
	Mn-siderite	Monazite	Monazite	Fluorapatite	Fluorapatite	Fluorapatite	Fluorapatite

Table 3: Stable isotope data of rocks from MMTU drill core (Michigan Technical University).

Identifier**	position (m)	$\delta^{13}C_{carb}$	err.	$\delta^{18}O_{carb-SMOW}$	$\delta^{18}O_{carb-PDB}$	err.	$\delta^{13}C_{org}$	TOC (wt%)
MMTU-4.40	1.3						-23.8	0.49
MMTU-4.5	1.4						-28.0	0.59
MMTU-5.69	1.7	-3.3	0.1	+20.7	-10.1	0.2	-23.2	0.23
MMTU-5.75	1.8	-4.6	0.1	+19.1	-11.6	0.2	-22.4	0.84
MMTU-6.25	1.9						-33.6	0.50
MMTU-6.6	2.0						-22.9	0.38
MMTU-7.3	2.2						-23.5	0.65
MMTU-8.6	2.6	-2.8	0.2	+20.5	-10.2	0.3	-23.9	0.24
MMTU-9.5	2.9	-3.1	0.0	+19.0	-11.8	0.1	-25.5	0.57
MMTU-10.8	3.3						-20.8	0.35
MMTU-11.6	3.5	-4.3	0.2	+15.6	-15.1	0.3	-46.7	0.21
MMTU-12.3	3.7						-25.4	0.25
MMTU-13.87	4.2	-3.3	0.2	+13.7	-16.8	0.3	-25.2	0.24
MMTU-17.7	5.4	-1.5	0.1	+13.9	-16.7	0.3	-25.0	0.32
MMTU-18.4	5.6	-2.8	0.2	+13.6	-16.9	0.3	-23.7	0.10
MMTU-20.5	6.2	-4.7	0.2	+13.5	-17.1	0.3	-26.8	0.48
MMTU-21.59	6.6						-31.8	0.84
MMTU-25.7	7.8	-2.2	0.1	+14.4	-16.2	0.1	-26.4	0.16
MMTU-28.2	8.6						-33.4	0.45
MMTU-32.7	10.0						-29.1	0.38
MMTU-38.0	11.6	-5.2	0.2	+10.8	-19.7	0.2	-24.4	0.16
MMTU-40.0	12.2						-29.1	0.55
MMTU-42.1	12.8	-2.9	0.1	+14.5	-16.1	0.5	-24.1	0.18
MMTU-44.0	13.4						-29.4	0.31
MMTU-45.9	14.0						-25.6	0.31
MMTU-48.6	14.8						-24.0	0.10
MMTU-52.3	15.9	-3.7	0.5	+14.9	-15.7	0.3	-26.9	1.24
MMTU-53.7	16.4	-3.7	0.1	+13.7	-16.9	0.1	-25.4	0.36
MMTU-60.0	18.3						-26.4	1.38
MMTU-61.7	18.8						-27.2	0.44
MMTU-63.3	19.3	-2.8	0.1	+15.4	-15.2	0.2	-28.4	0.41
MMTU-66.1	20.1						-28.0	0.37
MMTU-69.2	21.1						-25.1	1.45
MMTU-71.5	21.8						-23.2	0.27
MMTU-74.6	22.7	-2.9	0.2	+13.8	-16.8	0.2	-28.9	0.62
MMTU-75.8	23.1	-3.3	0.2	+14.2	-16.4	0.2	-24.5	0.67
MMTU-88.8	27.1			+17.3			-44.5	0.21
MMTU-93.0	28.3	-1.4	0.2	+15.0	-15.6	0.2	-23.3	0.30
MMTU-93.6	28.5	-2.0	0.2	+15.3	-15.3	0.2	-23.2	0.40
MMTU-94.9	28.9						-21.5	0.05
MMTU-96.0	29.3			+13.4			-20.9	0.10
MMTU-97.2	29.6						-21.2	0.19
MMTU-100.0	30.5	-2.5	0.1	+13.7	-16.8	0.2	-25.3	0.89
MMTU-102.0	31.1	-3.2	0.2	+13.3	-17.3	0.3	-25.1	0.99
MMTU-103.8	31.6	-2.5	0.1	+14.3	-16.3	0.2	-23.3	0.19
MMTU-105.1	32.0	-3.5	0.2	+16.4	-14.2	0.1	-25.0	1.35
MMTU-106.7	32.5						-27.4	0.26
MMTU-107.8	32.9	-3.0	0.2	+14.0	-16.6	0.2	-26.5	0.30
MMTU-111.9	34.1	-3.6	0.1	+14.5	-16.0	0.2	-27.1	0.08
MMTU-115.8	35.3	-3.4	0.0	+11.8	-18.5	0.2	-22.3	0.19
MMTU-124.0	38.0	-3.6	0.1	+11.8	-18.7	0.4	-22.6	0.16
MMTU-127.3	38.8						-22.1	0.05
MMTU-129.5	39.5	-1.5	0.1	+14.4	-16.1	0.2	-23.4	0.12
MMTU-129.8	39.6	-2.7	0.1	+14.0	-16.6	0.1	-25.3	1.23
MMTU-130.5	39.8	-3.0	0.2	+12.7	-17.8	0.3	-23.4	0.05
MMTU-132.1	40.3						-30.4	0.08
	max	-1.4		+20.7	-10.1		-20.8	1.4
	min	-5.2		+10.8	-19.7		-46.7	0.0
	average	-3.1		+14.8	-15.8		-26.2	0.4
	stdev	0.9		2.3	2.3		4.8	0.4

* Sample name includes the depth (in feet, as originally measured) for each sample.

Table 4: Summary table of observations for the mineralogically distinct cherts of the Lake Superior Area.

	Gunflint – Organic (Prehnite-pumpelleyite facies)	**Biwabik – Hematitic (Sub-Greenschist facies)**	**Michigamme – Phosphatic (Greenschist facies)**
Size and morphology of stromatolites	Finely laminated columnar and columnar branching with diameter of 0.5 to 3 cm; intercolumnar granules	Columnar branching with diameter of 0.5 to 3 cm; intercolumnar granules	Coarsely laminated domal and turbinate with diameter of tens of cm
Mineralogy of stromatolites	Chert, OM, carbonate, apatite, pyrite hematite	Chert, hematite, carbonate, apatite, OM	Chert, carbonate, apatite, OM, pyrite, hematite
Size and morphology of granules	Ca. 120 to 1200 μm; sub-spheroidal to sub-ellipsoidal; most have fine concentric lamination	Ca. 150 to >2000 μm; sub-ellipsoidal to sub-angular , varied coarse-grained to fine-grained, some concentric	Ca. 200 to >2000 μm; sub-spheroidal to sub-hexagonal; most have a network of OM as regular pattern interior
Mineralogy of granules	Chert + OM + carbonate ± hematite ± pyrite ± greenalite	Chert + hematite ± OM ± Mn-dolomite ± apatite (some monazite) ± stilpnomelane ± greenalite ± vermiculite	Chert + apatite + OM ± hematite ± muscovite ± anatase ± magnetite ± pyrite
Size and morphology of rosettes	Ca. 25 to 100 μm[5]	?	Ca. 30 to 200 μm, sub-spheroidal with finely concentric laminations
Mineralogy of rosettes	Ankerite+siderite, apatite+chert[5]	Chert + hematite, siderite	Muscovite + apatite, and dolomite + OM
Size and morphology of filamentous microfossils	Diameter: 1-3 μm; length: >200 μm and curved to straight (*Gunflintia minuta*[1])	Diameter: 0.5-4 μm; length: >200 μm mostly straight, some curved (*Gunflintia minuta*[1])	Diameter: 2-6 μm; length: >200 μm and curved to straight (*Gunflintia minuta*[1])
Mineralogy of filamentous microfossils	Nanoscopic OM, OM + pyrite[2], OM + phyllosilicate[3], carbonate[1],	Hematite + chert ± OM	OM + apatite, OM + pyrite
Size of coccoidal microfossils	3 to 25 μm	Generally 2 to 30 μm with some up to 80 μm	10 to 50 μm
Mineralogy of coccoidal microfossils	OM, OM + pyrite[2], OM + phyllosilicate[3], carbonate[1]	Hematite, hematite + OM	OM + apatite, OM +pyrite
Raman D-band parameters	Between 1339 and 1357 cm^{-1} with a FWHM between 90 and 130 cm^{-1}	Between 1337 and 1356 cm^{-1} with FWHM between 90 and 160 cm^{-1} (interference with hematite and epoxy)	Between 1338 and 1352 cm^{-1} with a FWHM between 44 and 65 cm^{-1}
Raman G-band parameters	Between 1586 and 1604 cm^{-1} with a FWHM between 45 and 57 cm^{-1}	Between 1569 and 1599 with FWHM between 58 and 80 cm^{-1}	Between 1566 to 1587 cm^{-1} with a FWHM between 41 and 77 cm^{-1}
Range of $\delta^{13}C_{carb}$ values	$\delta^{13}C_{carb}$ = -8.7 to -0.2‰ ([4]) $\delta^{18}O_{carb}$ = +15.2 to +24.6‰ ([4])	$\delta^{13}C_{carb}$ = -18.6 to -3.7‰ ([6]) $\delta^{18}O_{carb}$ = +12 to +20‰ ([6])	$\delta^{13}C_{carb}$ = -5.2 to -1.4‰ $\delta^{18}O_{carb}$ = +20.8 to +30.8‰

[1]Barghoorn and Tyler (1965), [2] Wacey et al. (2014), [3] Wacey et al. (2015), [4] Winter and Knauth (1992), [5] Heaney and Veblen (1990), [6] Perry et al., (1973).

Figure 1 – Papineau et al. (2017)

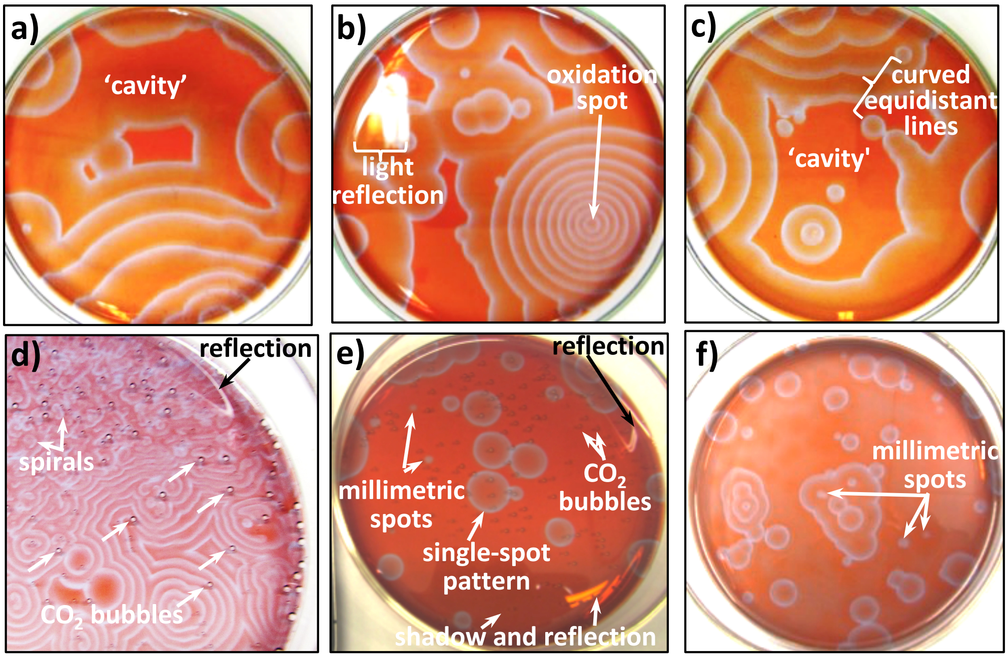

Figure 1: Reflected light images of different chemically-oscillating experiments performed with the same chemicals as in the classical Belousov-Zhabotinsky experiment (6ml of {67 ml (H_2O + 2 ml H_2SO_4 + 5g $NaBr0_3$} + 0.5ml of {1g NaBr + 10 ml H_2O} + 1ml of {1g Malonic acid + 10 ml H_2O} + 1ml of {25mM pheanthroline ferrous sulphate (or Ferroin (3 mM) – a coloured redox indicator} + 0.5ml of {1g Triton X-100 + 1000ml H_2O (to decrease surface tension)}. a) Formation of a 'cavity' from oxidation spots along the edge of the Petri dish (10 cm diameter), b) formation of oxidation spots and concentric oxidation fronts with characteristic rounded equidistant lines, c) curved equidistant lines forming a 'cavity' that encloses concentric oxidation spots, d) rounded oxidation spots with finely equidistant oxidation fronts and CO_2 bubble formation (white arrow), e) centimetre to millimetre-size single rounded spot pattern with CO_2 bubbles, f) individual millimetre-size spots inside centimetre-size non-circular structures.

Figure 2 – Papineau et al. (2017)

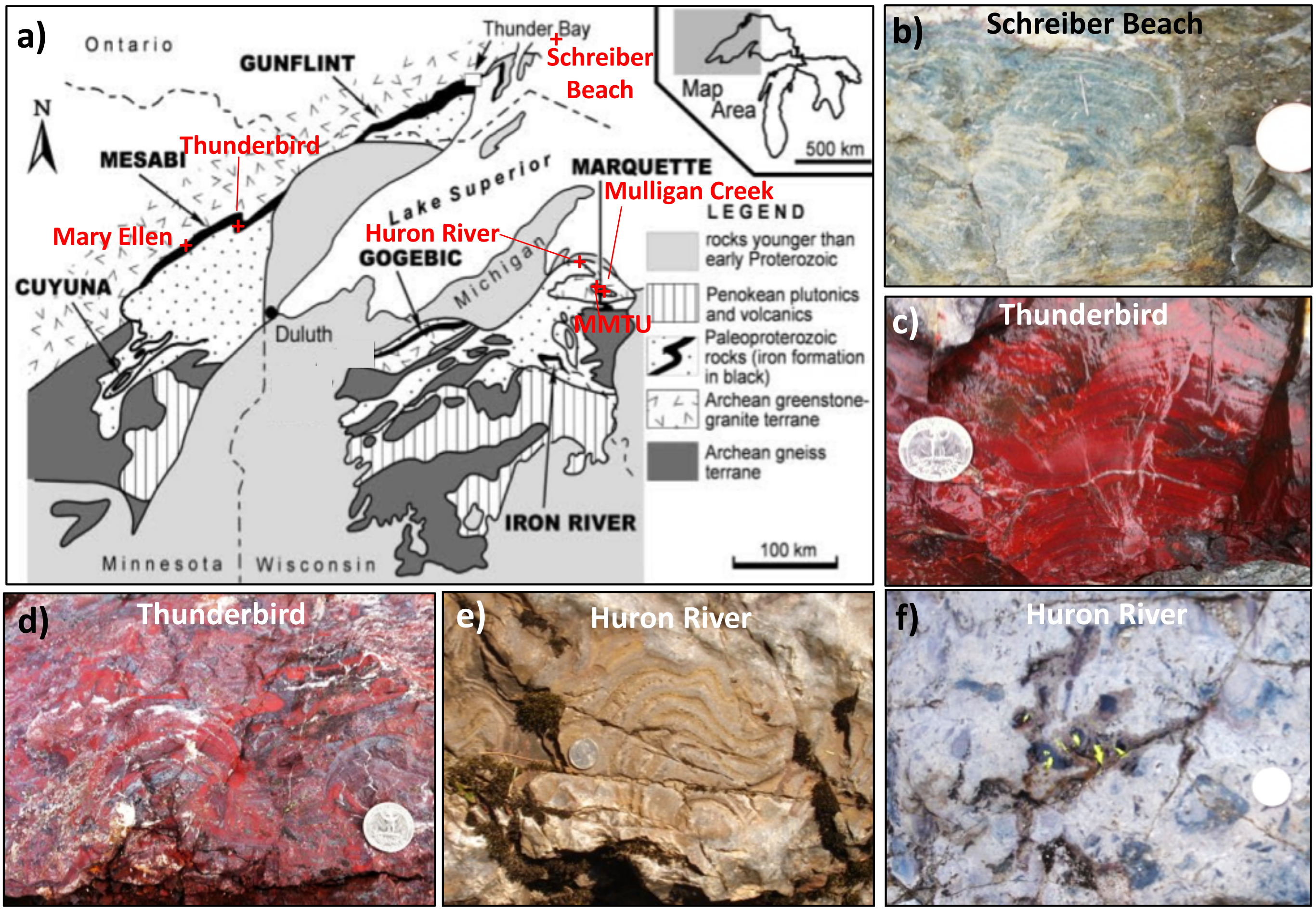

Figure 2: Geological context of the studied stromatolitic and concretionary cherts from the Gunflint, Biwabik, and Michigamme formations. a) regional geological map (modified from Pufhal and Fralick, 2004) showing the main iron ranges (bold) and the localities where samples from this study come from (red). Images of field outcrops of b) black chert from the Gunflint Fm. at the Schreiber Beach locality with centimeter-size columnar stromatolites, c) finely laminated columnar stromatolitic and granular jasper and d) bed of centimeter-size gray and red haematite-magnetite concretions with white carbonate patches in the Biwabik Fm., and e) coarse laminated decimeter-size cherty domal stromatolites and f) concretionary granular phosphatic chert stained yellow by ammonium molybdate from the Michigamme Fm. at the Huron River locality. Coin diameter is 19mm in b) and 24mm in c-f).

Figure 3 – Papineau et al. (2017)

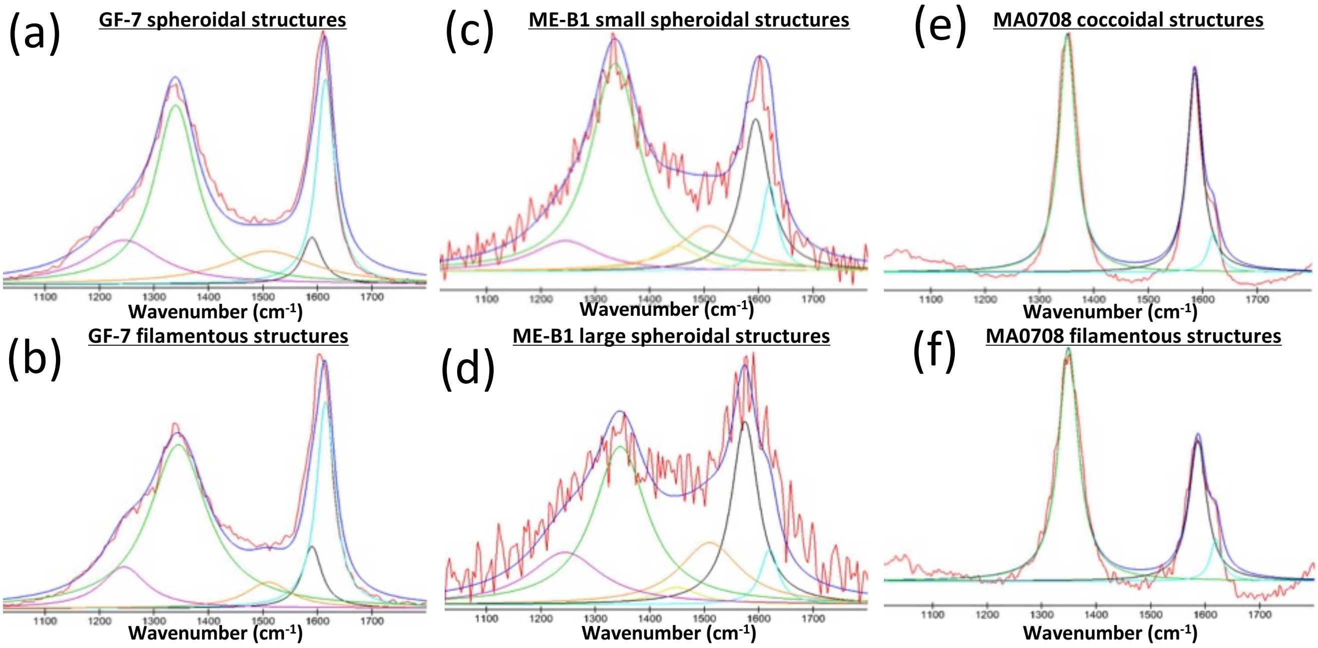

Figure 3: Measured (red) and modelled (blue) Raman spectra, after cosmic-ray reduction and polymonial-fitted background subtraction on OM from Gunflint, Biwabik, and Michigamme chert. Lorenz-fitted peaks are labelled in green (D1), turquoise (D2), orange (D3), purple (D4), yellow (D5), and black (G). Subsequent linear combination of lorenz-fitted D1, D2, D3, D4, D5, and G peaks is shown in blue - see calculated parameters in Table 1.

Figure 4 – Papineau et al. (2017)

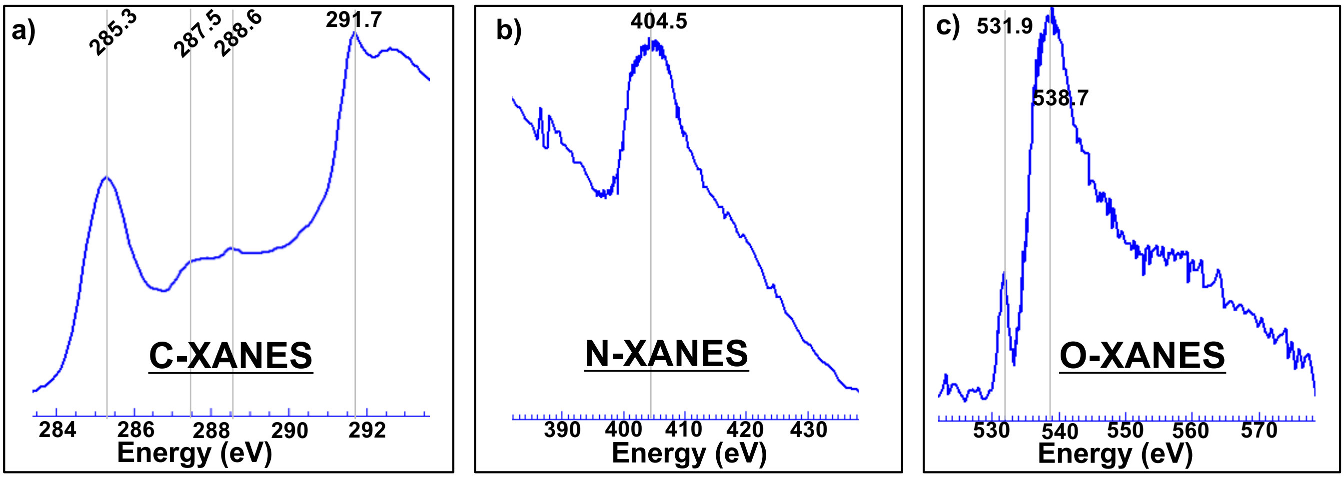

Figure 4: X-ray Absorption Near-Edge Structure spectra of acid-insoluble graphitic carbon from the Michigamme phosphatic chert *MA0708*. Spectrum in a) was acquired at C-edge and shows two strong peaks and two weak peaks, in b) shows a single weak peak at the N-edge, and in c) shows two peaks at the O-edge. The former XANES spectrum confirms the presence of carboxyl groups, while the latter two spectra confirm the presence of N and O functional groups in Michigamme graphitic carbon.

Figure 5 – Papineau et al. (2017)

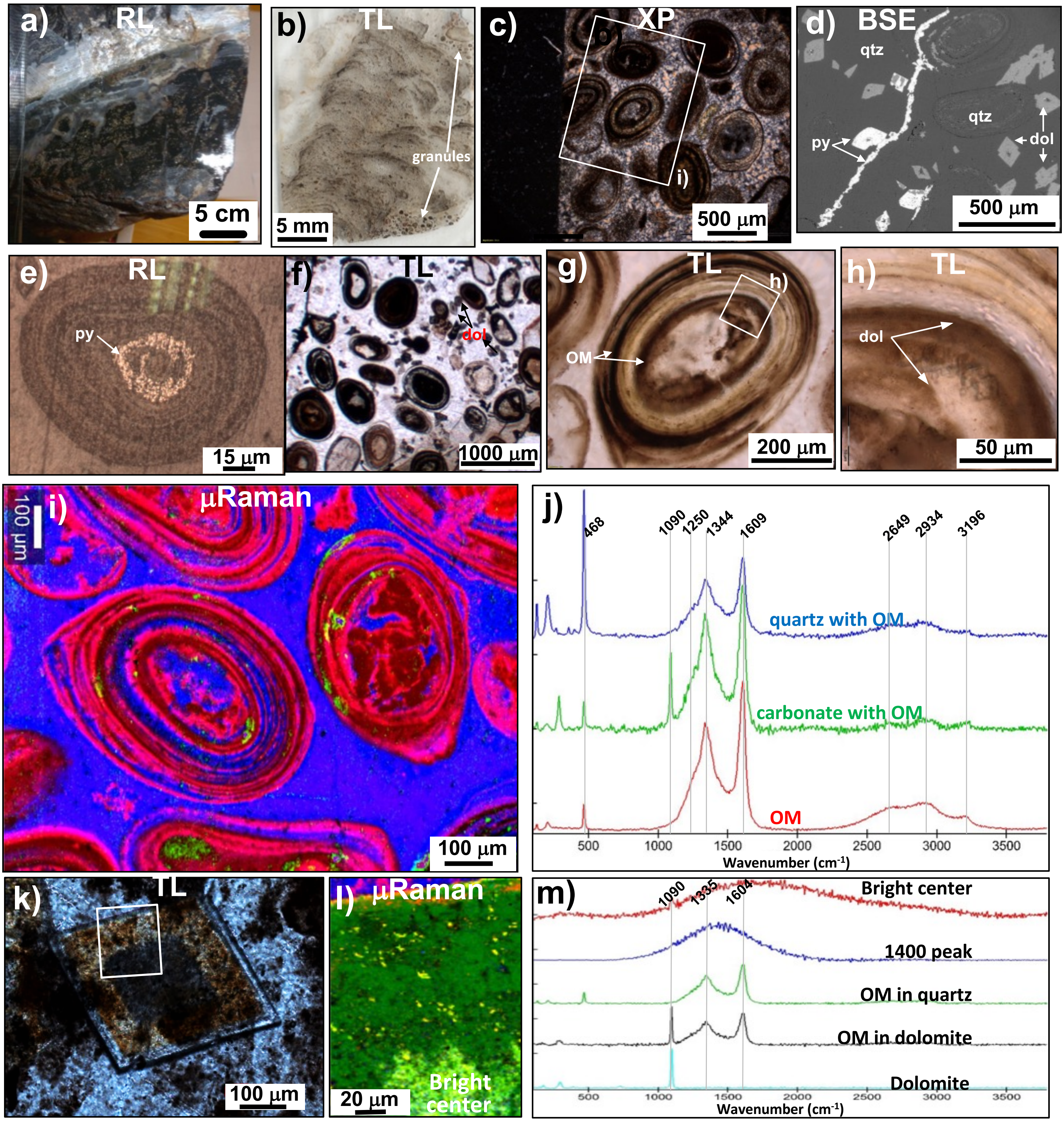

Figure 5: Petrography of stromatolitic and granular black chert sample *GF-1* from the Gunflint Formation. a) A slab of the Gunflint cherty columnar stromatolite below white chert layer, b) granules between stromatolitic chert columns with finely laminated OM, c) concentrically-laminated granules, d) intergranular dolomite rhombs, some almost completely replaced by later pyrite, e) concentrically-laminated granule with a nucleus coated with a spheroidal pyrite layer, f) Granules with dispersed dolomite rhombs, g-h) granule with finely laminated OM associated with dolomite shown by arrows in (h), i) micro-Raman image of several granules with carbonate associated with OM layers, j) Raman spectra for the three phases in (i) and (l), k-l) dolomite rhombohedron zoned with fluorescent OM, m) Raman spectra for dolomite rhomb. Raman colours here are the same for all subsequent figures: blue = quartz, green = carbonate, and red = OM. Abbreviations: BSE = Back-Scattered Electron, TL = transmitted light, CP = crossed polars, RL = reflected light, py = pyrite, dol = dolomite, qtz = quartz, OM = organic matter.

Figure 6 – Papineau et al. (2017)

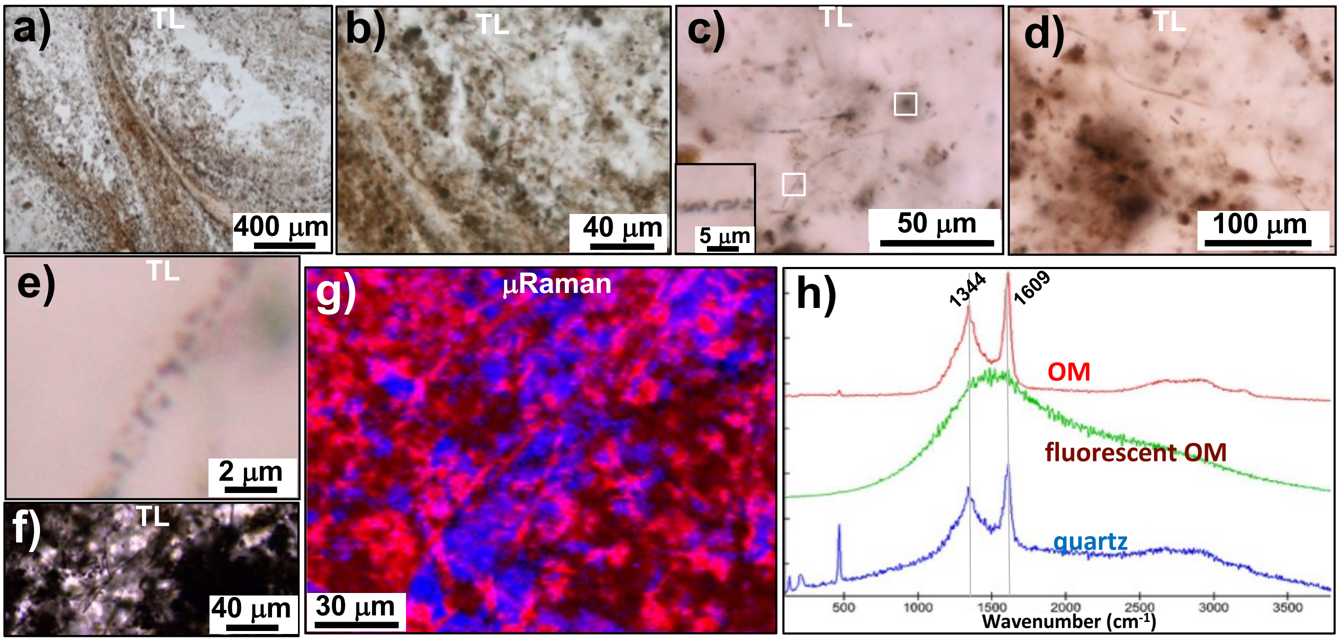

Figure 6: Petrography of filamentous structures composed of OM in black chert sample *GF-1* from the Gunflint Formation. a-b) Stromatolite laminations with filamentous structures, c-e) filaments of OM in the inter-columnar and intergranular matrix, f-g) filamentous structures composed of OM inside a granule, h) Raman spectra of OM along with occasional fluorescent regions.

Figure 7 – Papineau et al. (2017)

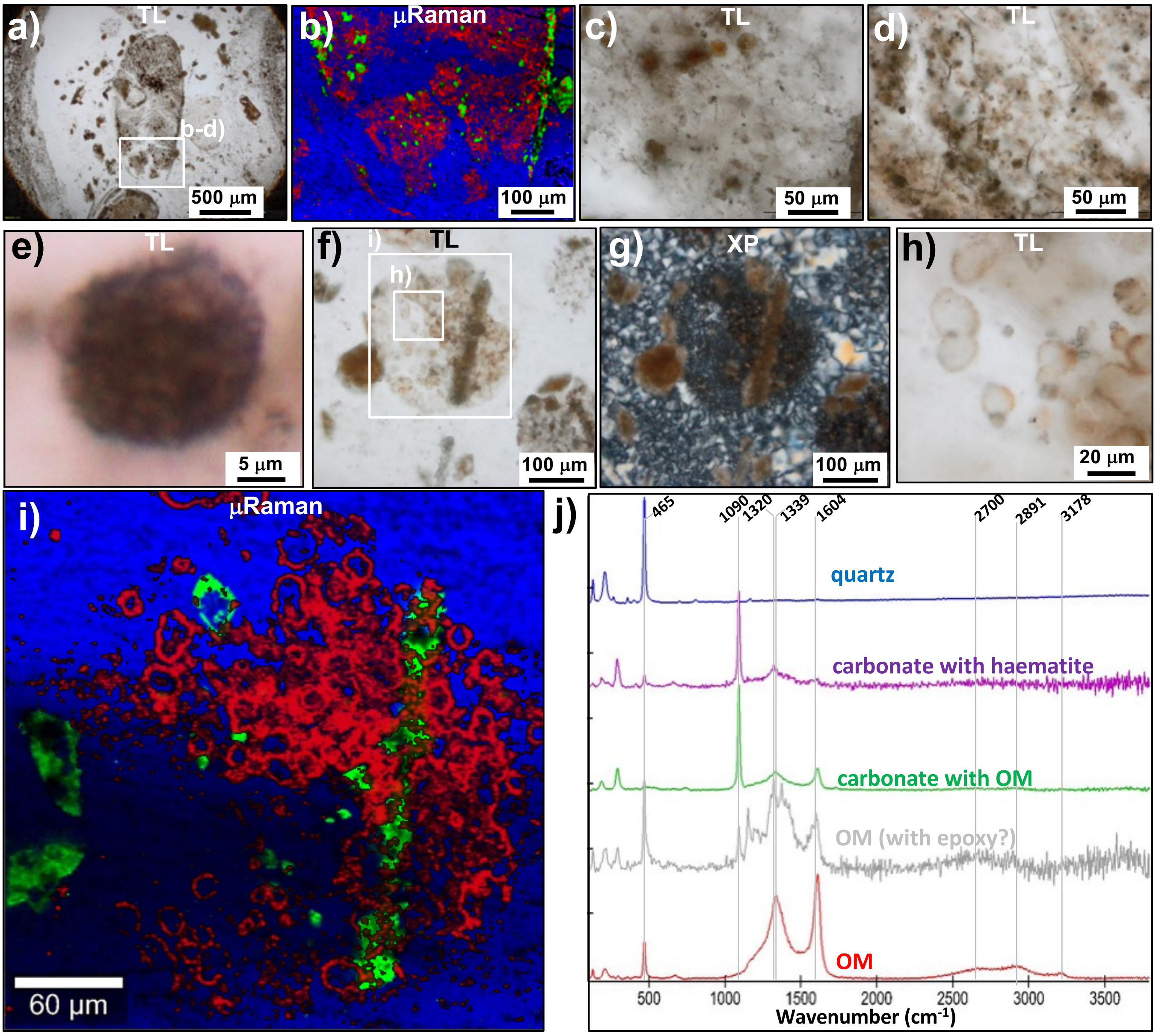

Figure 7: Examples of spheroidal structures in granules between columns of stromatolitic black chert from the Gunflint Fm (sample *GF-7*). a-c) granule with spheroidal and filamentous structures composed of OM, d) mixed spheroidal and filamentous structures in the chert matrix, e) spheroidal structure similar to *Huroniospora macroreticulata* in the matrix, f-h) granule with spheroidal structures and dolomite inside. i) Raman image of spheroidal structures composed of OM and carbonate in the granule in g), j) Raman spectra of the different phases in the Raman image.

Figure 8 – Papineau et al. (2017)

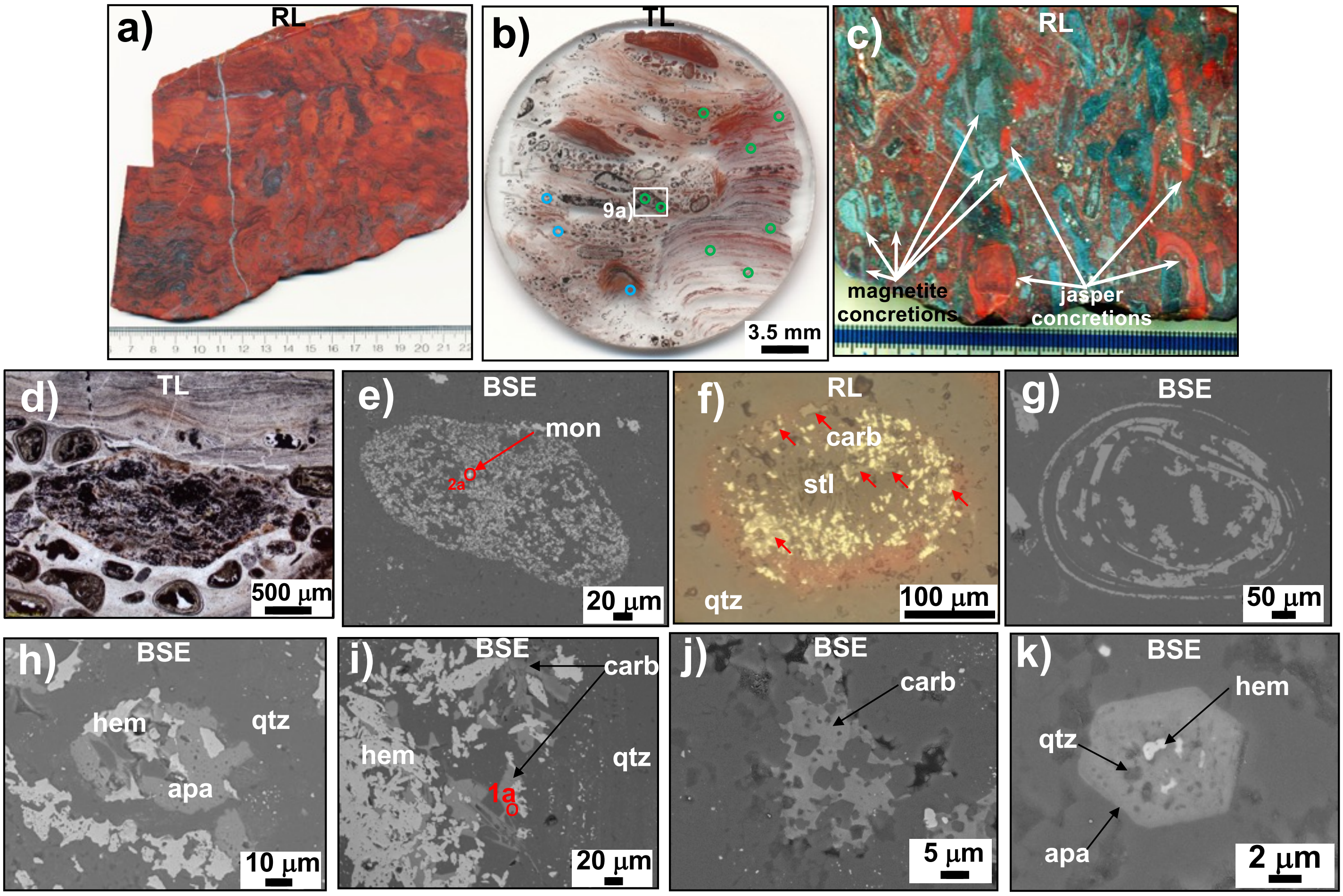

Figure 8: Petrography of stromatolitic and granular jasper from the Biwabik Fm (sample *ME-B1* – Mary Ellen locality) in all panels except c-d, which are from sample *AG1108* (Thunderbird locality). a) Polished slab of stromatolitic and granular jasper chert, b) thin section image of an area with intercolumnar granules and stromatolitic chert layered with microscopic red haematite showing the location of microscopic Mn-carbonate (blue circles) and apatite (green circles), c) polished slab of jasper with jasper and magnetite concretions, d) millimetre-size haematite-magnetite concretion amongst granules with fine internal disseminations of haematite forming wavy and spheroidal patterns, e) haematite granule with a grain of monazite, f) haematite granule with stilpnomelane core and anhedral carbonate (red arrows), g) haematite granule with fine concentric laminations, h) magnetite granule with blades of yellow-brown apatite, i) subhedral Mn-siderite in a coarse-grained haematite granule, j) anhedral Mn-siderite with poikilitic texture, k) euhedral apatite with nanoscopic inclusions of quartz and haematite inside a stromatolite column. Spot numbers (in red in panels e and m) are for EDS analyses listed in Table 2. Abbreviations: mon = monazite, hem = haematite, qtz = quartz, carb = carbonate, apa = apatite, stl = stilpnomelane.

Figure 9 – Papineau et al. (2017)

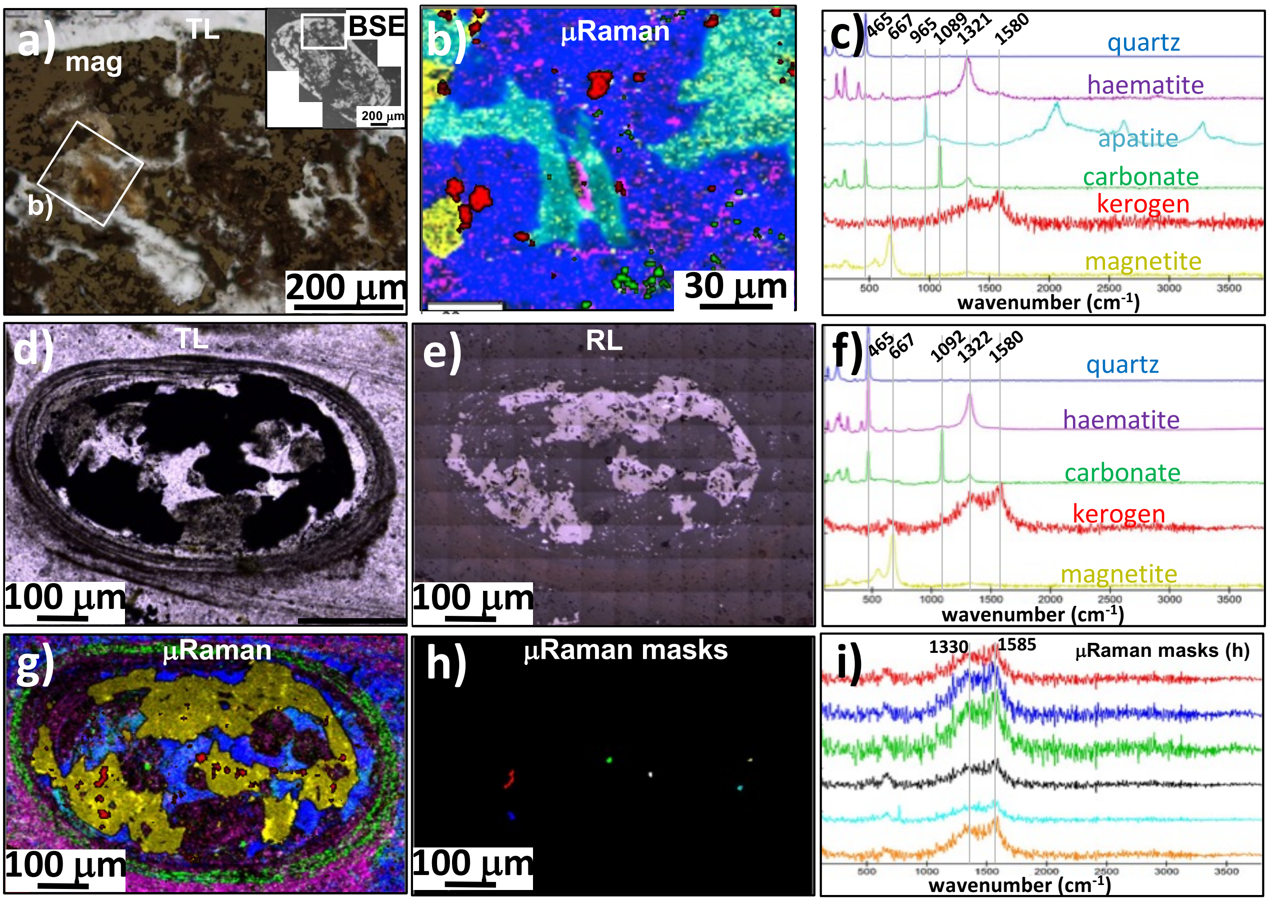

Figure 9: Detailed examples of occurrences of micron-size particles of OM in the Biwabik jasper-chert. (a-c) Apatite associated with carbonate and organic matter inside magnetite-haematite granule shown in inset. (d-g) Magnetite-haematite granule with coarse grained interior of quartz, magnetite, and haematite and with a rim of micron-size carbonate grains. (h-i) colour-coded masks corresponding to Raman image in (g) for micron-size particles of organic matter inside magnetite and related to their spectra in (i), most having low signal-to-noise ratio. Colours in Raman images are same as before along with yellow = magnetite, turquoise = apatite, and purple = haematite. mag = magnetite.

Figure 10 – Papineau et al. (2017)

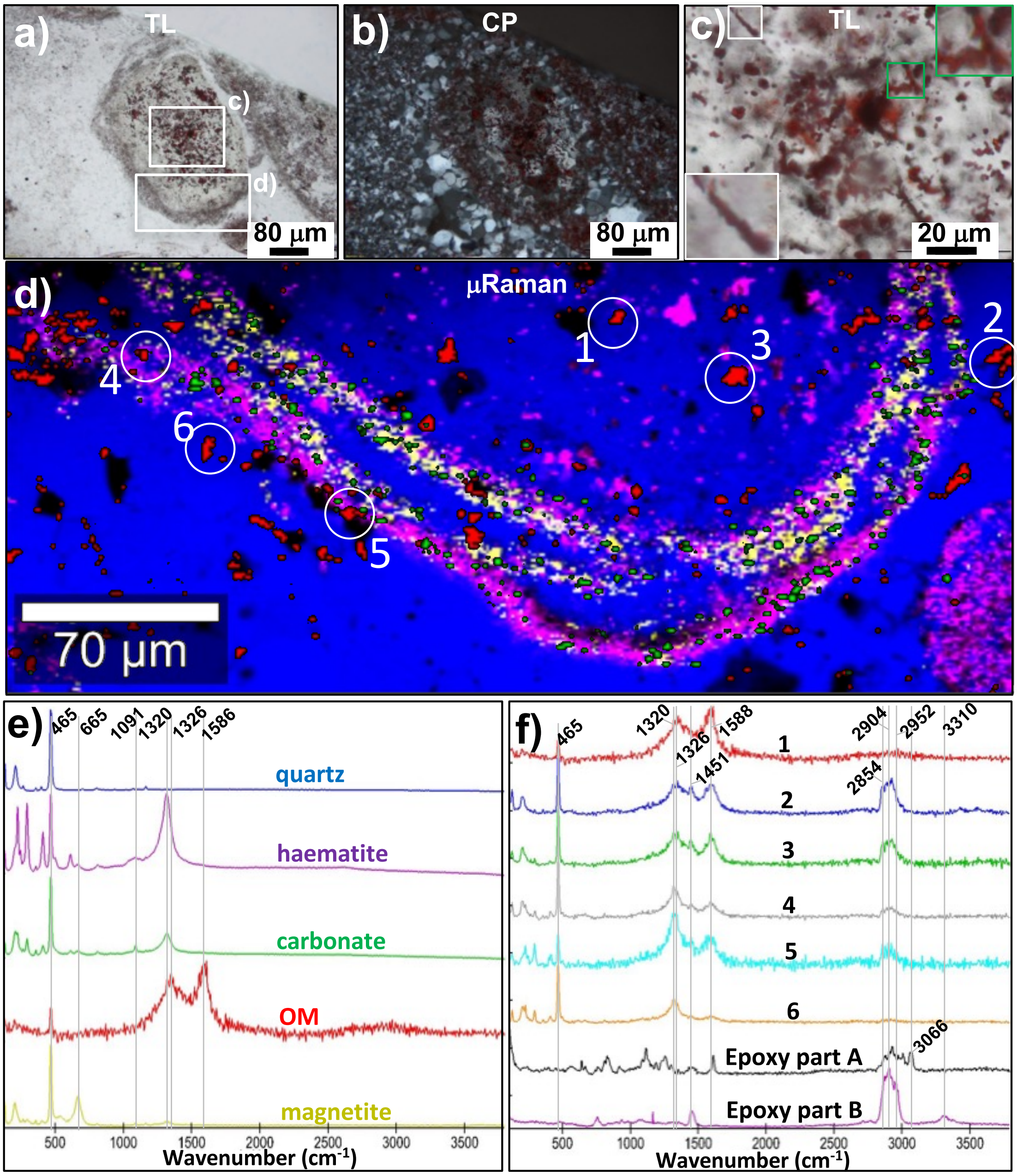

Figure 10: Filamentous structures in granular and stromatolitic jasper from the Biwabik Formation. a-c) Filamentous structures composed of haematite inside granules (with insets showing detailed view), d) Raman image of a section of the granule showing micron-size particles of OM, e) Raman spectra of the main minerals associated with this granule, f) diversity of Raman spectra for OM associated with haematite (numbers refer to OM particles circled in d).

Figure 11 – Papineau et al. (2017)

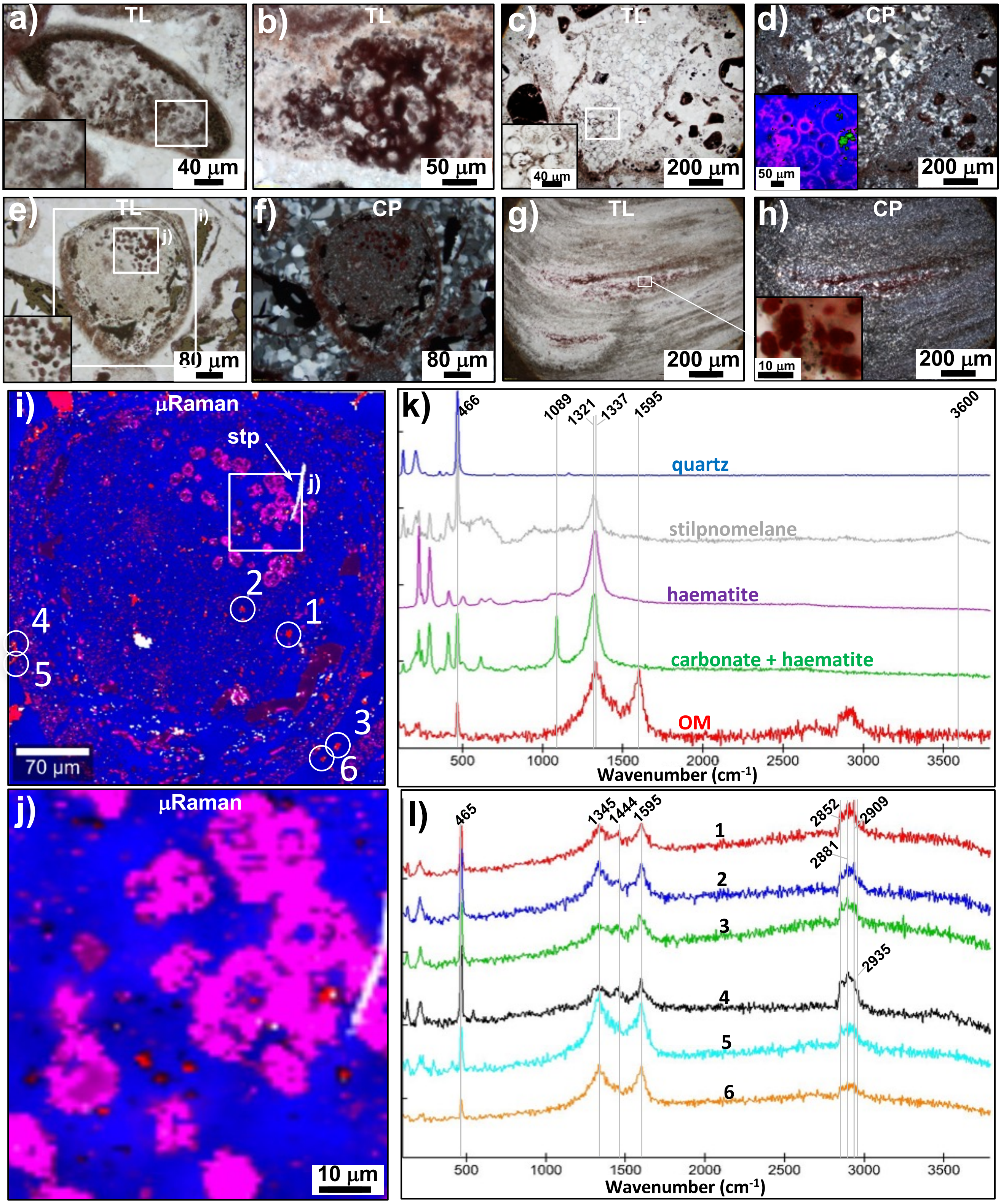

Figure 11: Spheroidal structures in granular and stromatolitic jasper from the Biwabik Formation. a-f) Spheroidal structures composed of haematite inside granules shown with zoomed-in insets, g) coarse grained chert interlayer in stromatolite column with micron-size spheroidal structures (shown in inset), i-j) Raman images of haematitic spheroidal microfossils associated with micron-size particles of OM, k) Raman spectra of the main minerals associated with spheroidal structures, i) range of Raman spectra for OM associated with haematite (numbers refer to those in i). colours in Raman image are same as in Fig. 9 with white = stilpnomelane.

Figure 12 – Papineau et al. (2017)

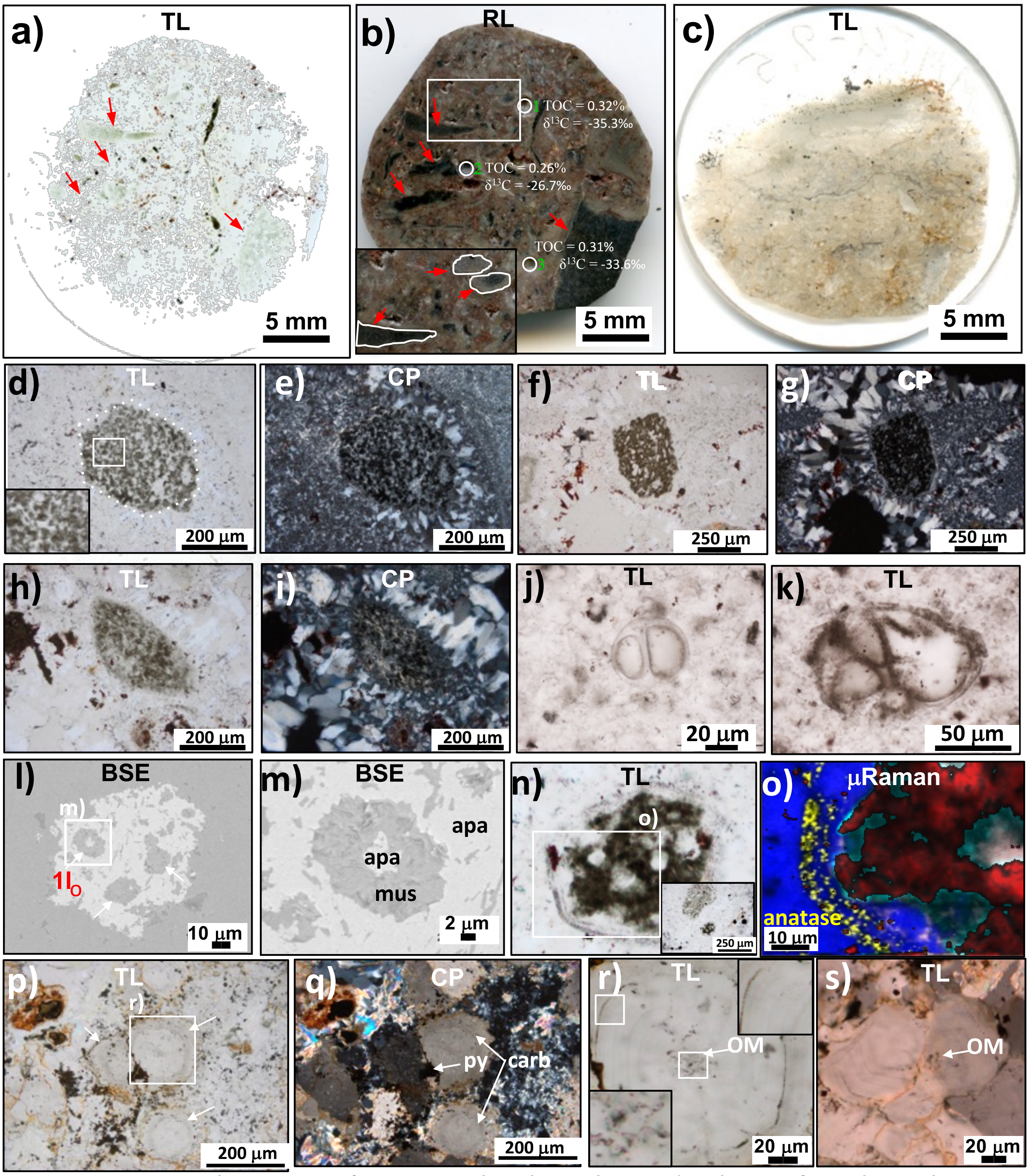

Figure 12: Petrographic context of apatite in phosphatic chert and carbonate from the Michigamme Fm. a-b) transmitted and reflected light images of sample *MA0708* (Huron River Locality) with arrows pointing to dark concretionary apatite structures, c) sample *MMTU-9.5* (Dead River Basin). Photomicrographs (d-o) are for *MA0708*: d-i) apatite granules with OM forming regular patterns shown in greater detail in inset for d), j-k) two examples of compartmentalized spheroidal structures composed of apatite and OM in intergranular matrix, l-o) sub-hexagonal granule of apatite-graphitic carbon along with muscovite-sericite rosettes (white arrows) and surrounded by rounded equidistant laminations of nanoscopic anatase (best seen in n and o (yellow)). Sample *MMTU-9.5*: p-s) zoned carbonate granules with concentric rounded equidistant laminations (white arrows) around a center of nanoscopic OM, and intergranular pyrite and Fe-oxide. Abbreviations same as before with mus = muscovite (sericite). Colours in Raman image are blue = quartz, red = graphitic carbon, turquoise = apatite, yellow = anatase. Spot number in panel l) is for an EDS analysis listed in Table 2.

Figure 13 – Papineau et al. (2017)

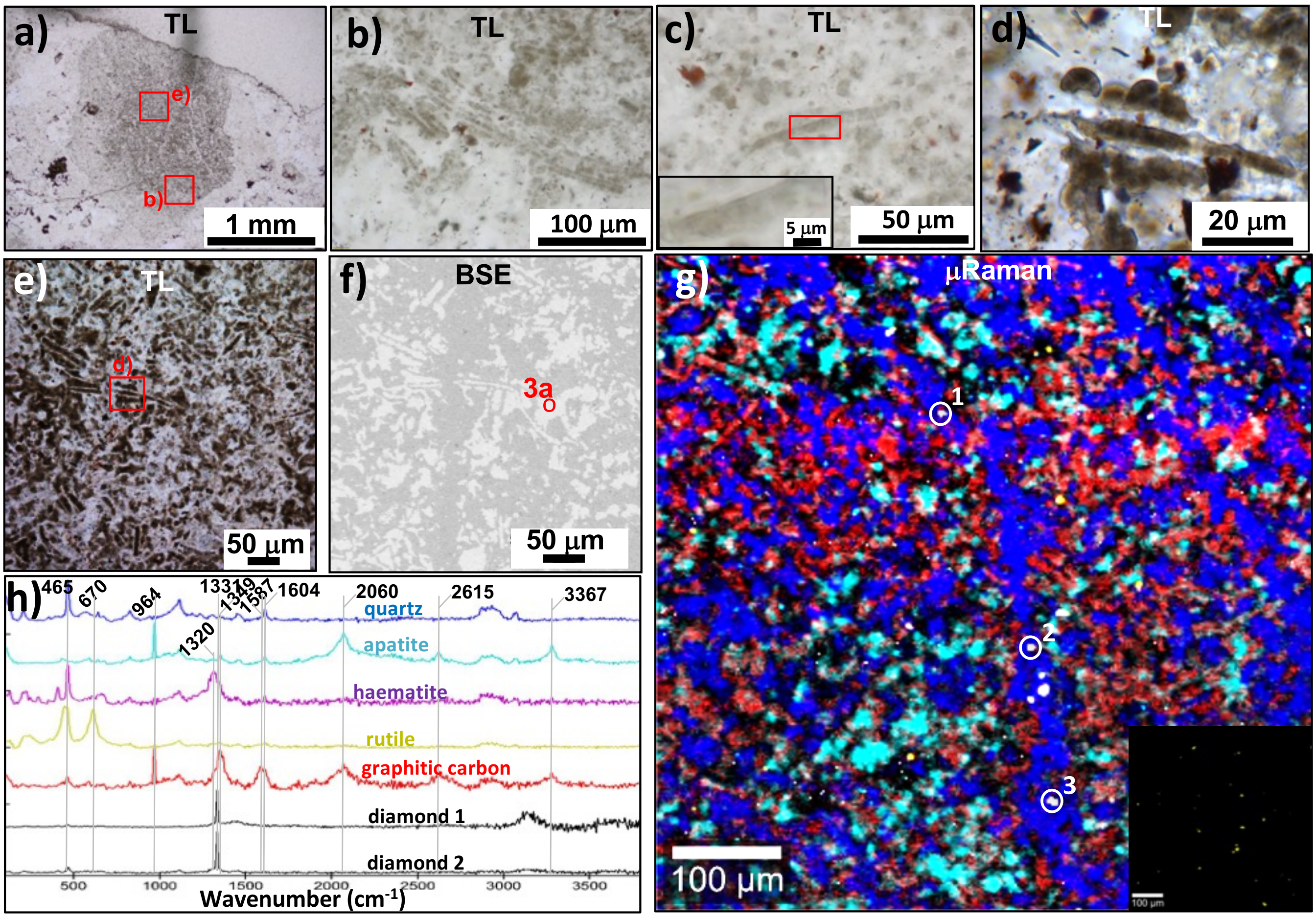

Figure 13: Filamentous structures composed of apatite with OM and associated with haematite and rutile in a granule from the Michigamme phosphatic chert (*MA0708*). a-f) Groups of filamentous structures composed of apatite and OM inside an apatite granule, g) Raman image of the apatite granule with filamentous structures (inset shows the 670 cm^{-1} filter for rutile in the same field), h) Raman spectra of the major minerals in this chert, along with detected contaminant diamonds. Colours are same as before and correspond between the hyperspectral image and the spectra, with purple = haematite and yellow = rutile. Spot number in red (in panel f) is for an EDS analysis listed in Table 2.

Figure 14 – Papineau et al. (2017)

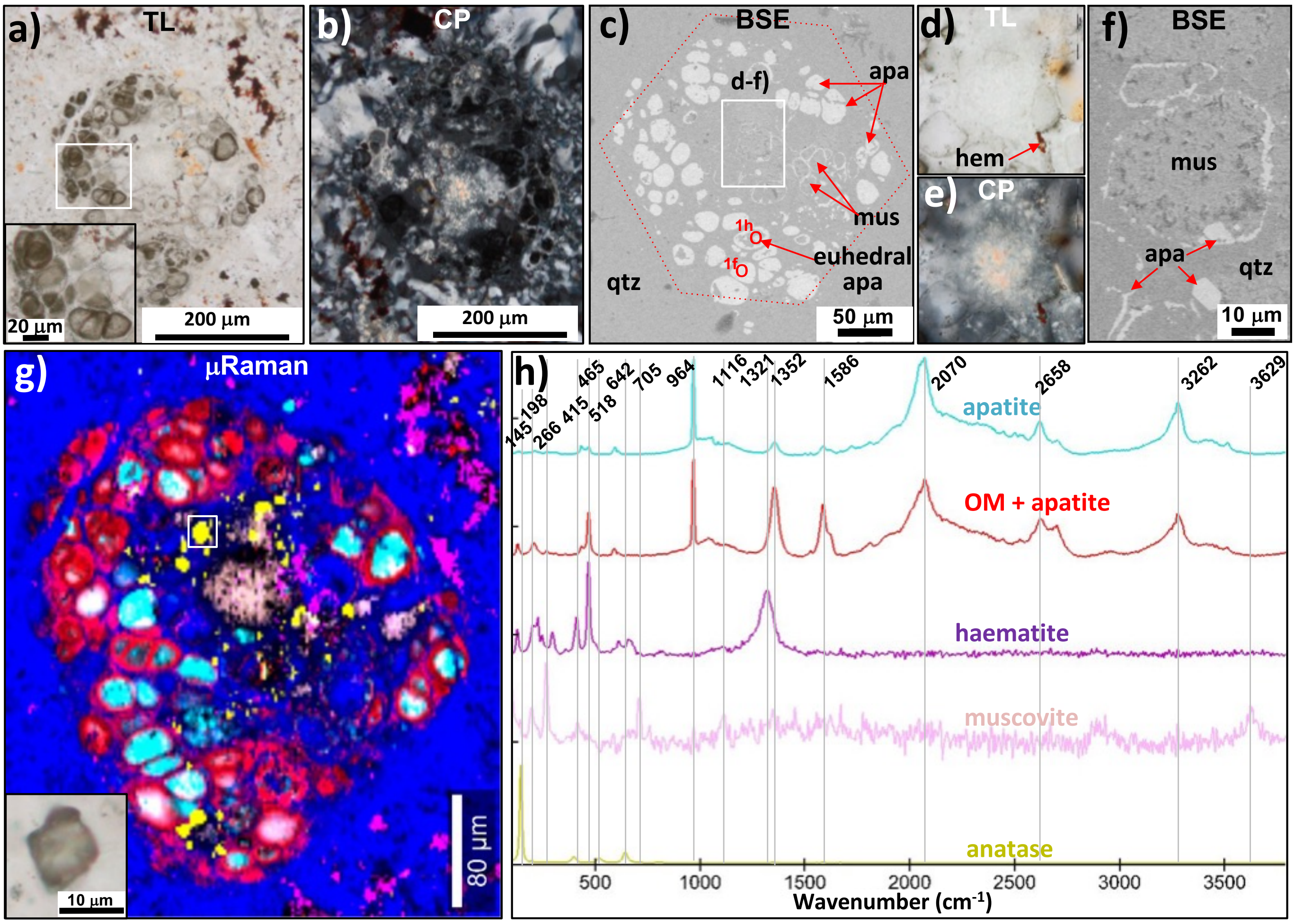

Figure 14: Spheroidal structure in a granule from the Michigamme phosphatic chert. a-c) Images of a granule that contains spheroidal structures composed of OM with apatite and that form an hexagonal shape (red dotted line in (c)), d-f) images of a muscovite rosette with a rim of apatite located near the center of the granule, g) Raman image of the different phases in this granule based on major peaks in Raman spectra shown in h). Spot numbers in red are for EDS analyses listed in Table 2. Mineral abbreviations and Raman colour codes are the same as before, and mus = muscovite. Colours in Raman image are same as Fig. 12 with pink = muscovite.

Figure 15 – Papineau et al. (2017)

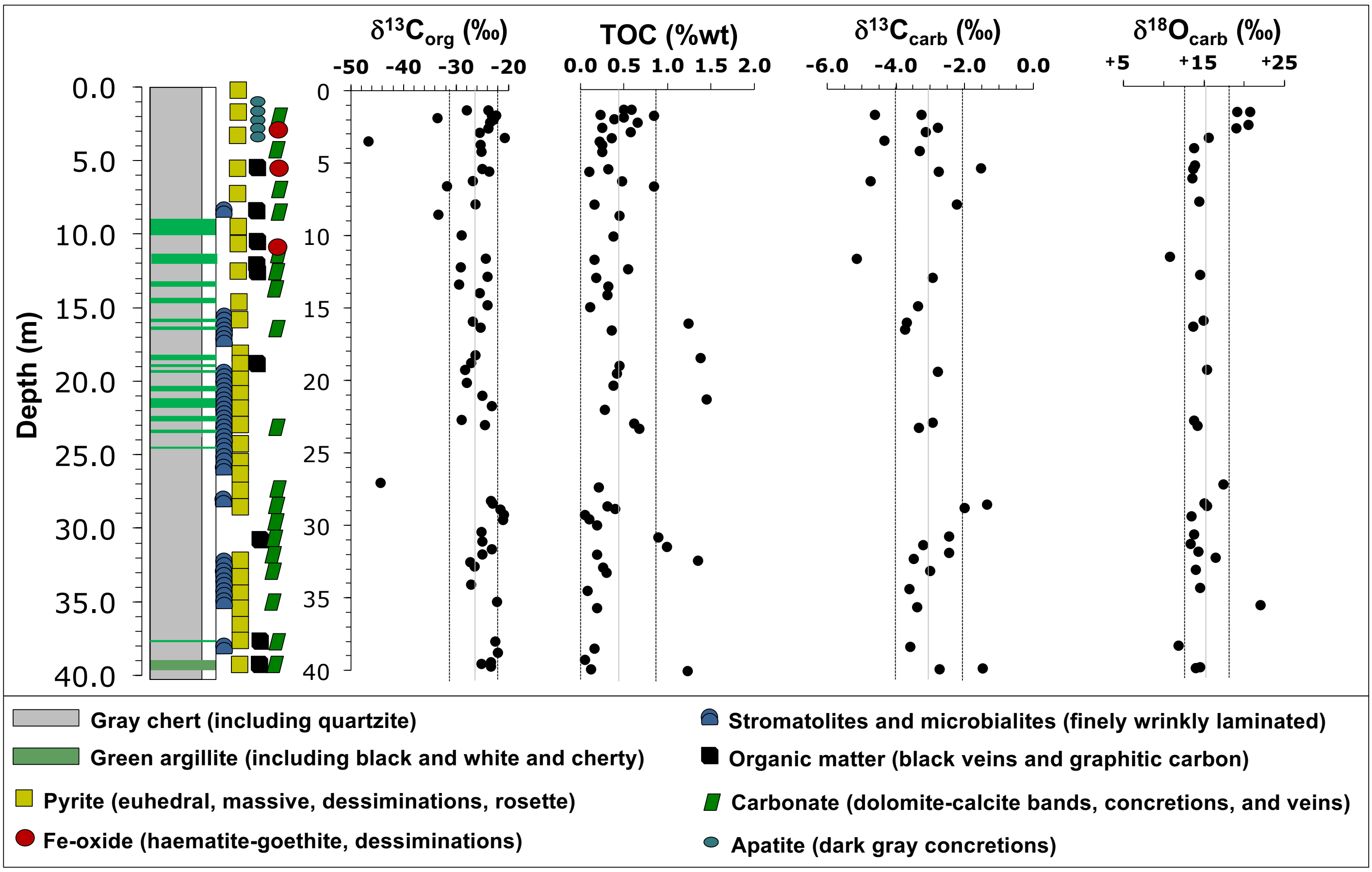

Figure 15: Chemostratigraphic profile of the MMTU drill core from the Michigamme Fm with carbon isotope composition of acid-insoluble OM, total organic carbon (TOC), and carbon and oxygen isotope compositions of carbonate. Vertical lines show averages (light gray) and 1σ standard deviations (black). Stratigraphic details modified from IMR drill core log (Mulligan Plains, Sec. 15, R28W, T49N, Marquette County, Michigan).

Figure 16 - Papineau et al. (2017)

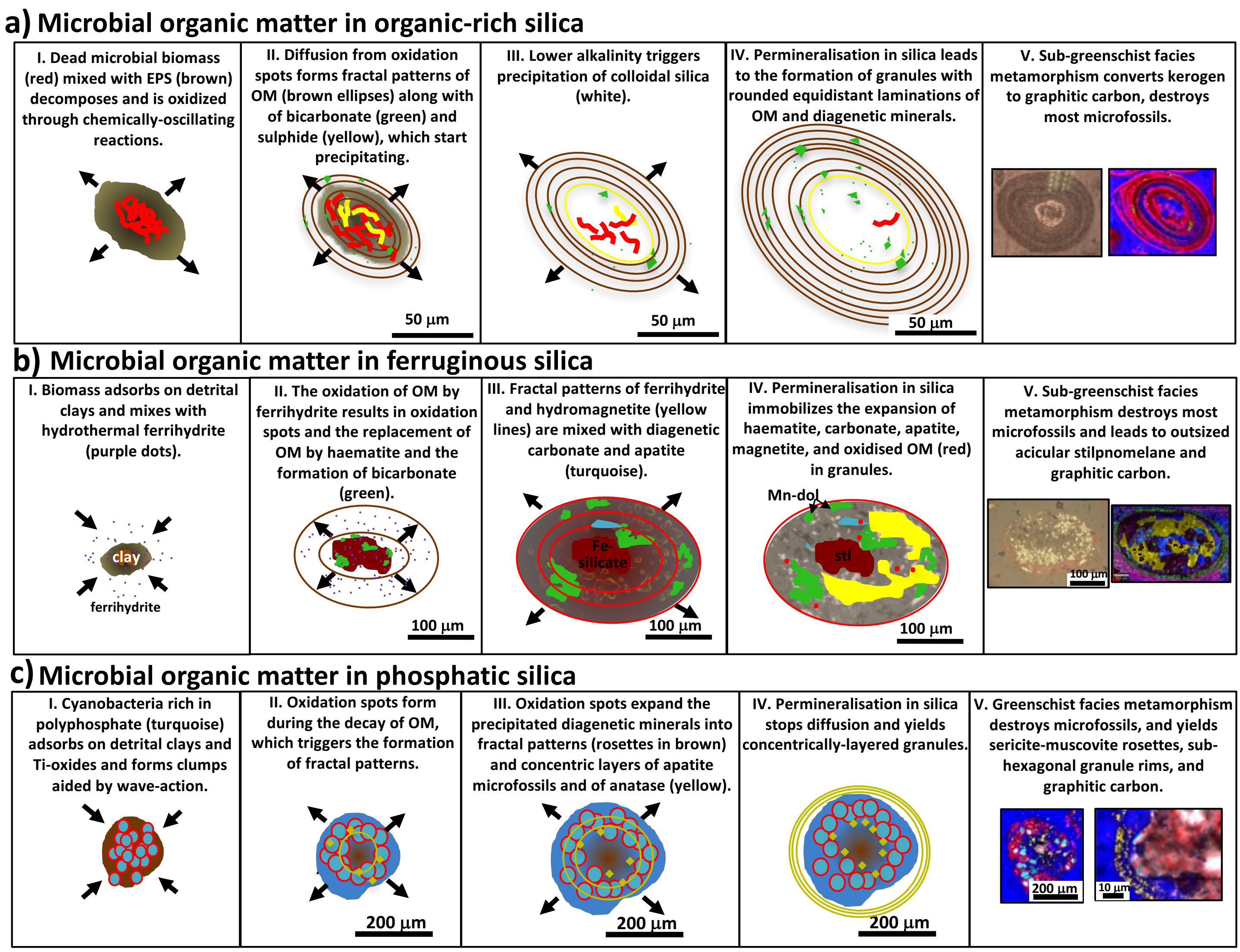

Figure 16: Proposed models for the diagenetic growth of granules from the non-biological oxidation of organic matter in a) organic granular chert (e.g. in Gunflint Fm), b) haematite-rich chert (e.g. in Biwabik Fm), and phosphatic and clay-rich granular chert (e.g. in Michigamme Fm).